



HAL
open science

How galaxy properties vary with filament proximity in the SIMBA simulations

Teodora-Elena Bulichi, Romeel Davé, Katarina Kraljic

► **To cite this version:**

Teodora-Elena Bulichi, Romeel Davé, Katarina Kraljic. How galaxy properties vary with filament proximity in the SIMBA simulations. *Monthly Notices of the Royal Astronomical Society*, 2024, 529, pp.2595-2610. 10.1093/mnras/stae667. insu-04522995

HAL Id: insu-04522995

<https://insu.hal.science/insu-04522995v1>

Submitted on 27 Mar 2024

HAL is a multi-disciplinary open access archive for the deposit and dissemination of scientific research documents, whether they are published or not. The documents may come from teaching and research institutions in France or abroad, or from public or private research centers.

L'archive ouverte pluridisciplinaire **HAL**, est destinée au dépôt et à la diffusion de documents scientifiques de niveau recherche, publiés ou non, émanant des établissements d'enseignement et de recherche français ou étrangers, des laboratoires publics ou privés.



Distributed under a Creative Commons Attribution 4.0 International License

How galaxy properties vary with filament proximity in the SIMBA simulations

Teodora-Elena Bulichi¹   ¹★ Romeel Davé^{1,2,3}  and Katarina Kraljic⁴

¹*Institute for Astronomy, University of Edinburgh, Royal Observatory, Blackford Hill, Edinburgh EH9 3HJ, UK*

²*University of the Western Cape, Bellville, Cape Town 7535, South Africa*

³*South African Astronomical Observatories, Observatory, Cape Town 7925, South Africa*

⁴*Observatoire Astronomique de Strasbourg, Université de Strasbourg, CNRS, UMR 7550, F-67000 Strasbourg, France*

Accepted 2024 March 1. Received 2024 February 22; in original form 2023 September 1

ABSTRACT

We explore the dependence of global galaxy properties in the SIMBA simulation as a function of distance from filaments identified using DISPERSE. We exclude haloes with mass $M_h > 10^{13} M_\odot$ to mitigate the impact of group and cluster environments. Galaxies near filaments are more massive and have more satellites, which we control for by examining deviations from best-fitting scaling relations. At $z = 0$, star formation (SF) is significantly suppressed within $\lesssim 100$ kpc of filaments, more strongly for satellites, indicating substantial pre-processing in filaments. By $z = 2$, the trend is weak and if anything indicates an increase in SF activity close to filaments. The suppression at $z \lesssim 1$ is accompanied by lowered HI fractions, and increased metallicities, quenched fractions, and dispersion-dominated systems. H_2 fractions are not strongly suppressed when controlling for stellar mass, suggesting that SF efficiency drives the drop in SF. By comparing amongst different SIMBA feedback variant runs, we show that the majority of SF suppression owes to filamentary shock-heating, but there is a non-trivial additional effect from AGN feedback. When looking around massive ($M_h > 10^{13} M_\odot$) haloes, those galaxies near filaments behave somewhat differently, indicating that filaments provide an additional environmental effect relative to haloes. Finally, we compare SIMBA results to EAGLE and IllustrisTNG at $z = 0$, showing that all models predict SF suppression within $\lesssim 100$ kpc of filaments, none the less, detailed differences may be observationally testable.

Key words: methods: numerical – galaxies: evolution – large-scale structure of Universe.

1 INTRODUCTION

The Universe on large scales is comprised of a network of galaxies, gas and dark matter forming the so-called cosmic web (e.g. Bond, Kofman & Pogosyan 1996; Aragón-Calvo, van de Weygaert & Jones 2010). This large-scale structure (LSS) consisting of void regions, sheet-like walls, filaments, and nodes is predicted by the Zel’dovich’s model for the gravitational collapse of ellipsoidal fluctuations in the matter density field (Zel’dovich 1970a,b). The features of the cosmic web have been brought to light via systematic galaxy redshift surveys (e.g. de Lapparent, Geller & Huchra 1986, 1989; Colless et al. 2001; Tegmark et al. 2004), and are also supported by simulations which predict the hierarchical formation of voids, walls, and filaments assuming the well-established cold dark matter (CDM) paradigm (e.g. Springel 2005).

Within the cosmic web, galaxies continuously grow and evolve, their properties being strongly correlated with their local environments. Denser environments show overabundances of massive haloes due to the enhanced dark matter densities and the protohalo’s earlier collapse (e.g. Bond, Kofman & Pogosyan 1996), which favours the formation of massive galaxies. Such environments also appear to

have non-negligible effects on galaxies, even when controlling for galaxy masses, giving rise to the long-observed morphology–density and colour–density relations (Dressler 1980, 1986; Postman & Geller 1984; Kauffmann et al. 2004; Baldry et al. 2006; for reviews see Boselli & Gavazzi 2006, 2014).

Traditionally, environmental effects have been studied by contrasting galaxies within groups and clusters versus those in the ‘field’. In such studies, the environment is a proxy for halo mass, with dense environments representing massive haloes with virial mass $\gtrsim 10^{13} M_\odot$. Yet, the field population itself may not be homogeneous in terms of its environmental dependence. For instance, field galaxies within a filamentary environment could have enhanced galaxy growth due to the greater availability of gas relative to void regions, or else could be retarded if that gas were shock-heated on LSS. The filamentary web may be the site of ‘pre-processing’, in which galaxy properties are altered prior to entering into group and cluster environments (e.g. Fujita 2004; Wetzel et al. 2013). Disentangling these effects is important for fully characterizing the role of the environment in galaxy evolution.

However, identifying the imprint of the cosmic web on galaxy properties beyond the dominant effect of local density and mass has been shown to be a daunting task. Early observational works struggled to find clear evidence of such signature. Among them, Alpaslan et al. (2015) found that the galaxies’ properties are primarily

* E-mail: teob1823@mit.edu

influenced by stellar mass, rather than the environment. Additionally, Eardley et al. (2015) suggested that the observed cosmic web environmental effects on galaxy properties can be explained solely by their corresponding local densities. These contradicting results may be partly explained by the inability to properly distinguish between the effects of present local densities and past large-scale environments, given their strong correlation. To sort out these issues, it is of crucial importance to distinguish between mass- and environmental-driven effects, as well as clearly separate group- and cluster-like environments from large-scale cosmic web features.

From galaxy surveys, there is substantial evidence that galaxies close to filaments are more massive and show lower levels of star formation (SF). This has been shown using the Sloan Digital Sky Survey (SDSS; Abazajian et al. 2009) by Chen et al. (2017), Kuutma, Tamm & Tempel (2017), Poudel et al. (2017), using the VIMOS Public Extragalactic Redshifts Survey Multi- λ Survey (VIPERS-MLS; Moutard et al. 2016; Scodreggio et al. 2018) by Malavasi et al. (2017), using COSMOS-2015 (Laigle et al. 2016) by Laigle et al. (2018), using the Galaxy and Mass Assembly survey (GAMA; Driver et al. 2009) by Alpaslan et al. (2015), Kraljic et al. (2018), and using the WISExSuperCOSMOS survey (Bilicki et al. 2016) by Bonjean et al. (2020) (but see Darvish et al. 2014; Vulcani et al. 2019, for observational results finding enhanced levels of (specific) SF in the proximity of filaments). These mass and SFR trends have also been supported several studies focused on cosmic voids showing that galaxies residing within them tend to be less massive, bluer, and more star forming (e.g. Grogin & Geller 2000; Rojas et al. 2004; Kreckel et al. 2011; Hoyle, Vogeley & Pan 2012; Beygu et al. 2016) compared to higher density environments (but see Ricciardelli et al. 2014; Kreckel et al. 2015; Wegner et al. 2019, for claims on no significant impact of void environment on galaxy properties).

Galaxy formation simulations within a cosmological context should naturally yield such environmental trends as a consequence of the interplay between galaxy accretion and LSS. However, again, the results are mixed. Kraljic et al. (2018) and Malavasi et al. (2022) investigated galaxy properties near filaments using the HORIZON-AGN (Dubois et al. 2014) and ILLUSTRISTNG (Pillepich et al. 2018) simulations, respectively, and generally reported suppressed SF in agreement with some observational results. On the other hand, when looking at high- z massive dense filaments and dwarf galaxies, Zheng et al. (2022) found a slight increase in the SFR, using the Auriga simulations (Grand et al. 2017). Additionally, Kotecha et al. (2022) found that galaxies close to filaments tend to be more star forming when looking at simulated clusters from the Three Hundred Project (Cui et al. 2018). This proves once again that, apart from the different prescriptions of simulations, the sample selection and environment classification play a vital role in such analyses too. Reconciling all these results likely requires considering survey selection effects and the specific techniques used to characterize filamentary structure, but in principle, the properties of galaxies within the filamentary LSS should provide a novel test of galaxy formation models.

Other properties have also been investigated in terms of the cosmic web environment. Kuutma, Tamm & Tempel (2017) and Poudel et al. (2017) showed using SDSS that at fixed environment density, the elliptical fraction is higher close to filaments. Poudel et al. (2017) proposed that the differences in galaxy SF properties result from the higher abundances of elliptical galaxies close to filaments. A similar result was also observed by Castignani et al. (2022), when looking out to 12 virial radii from the Virgo cluster. Salerno et al. (2020), using the Six Degree Field Galaxy Survey (6dFGS, Jones et al. 2004), found that galaxies arriving at clusters by following filaments are more quenched than galaxies that accrete on to clusters

isotropically (see also Gouin et al. 2020 and Malavasi et al. 2022). While these results suggest that the morphology–density and colour–density relations are established during the pre-processing phase, they are still focused on the vicinity of massive haloes rather than the full cosmic web.

Gas and metal content have also been explored in terms of the filamentary web. For the atomic hydrogen content in galaxies (H I), Kleiner et al. (2017) and Crone Odekon et al. (2018) reported different results. Kleiner et al. (2017) showed, using the 6dFGS that galaxies more massive than $M_* > 10^{11} M_\odot$ show higher H I to stellar mass ratio (H I fraction) near filaments, while no trend is observed for lower mass galaxies. Crone Odekon et al. (2018) used the ALFALFA H I survey (Giovanelli et al. 2005) to show that the H I fraction increases at increasing distance from filaments, at fixed local density and stellar mass. These last results are supported by Castignani et al. (2022), who added that the molecular hydrogen (H_2) does not show a clear trend with respect to the distance from filaments. For metallicity, this has only been explored in both observations and simulations, with Winkel et al. (2021) reporting that centrals in SDSS are more metal-enriched close to cosmic web structures and Donnan, Tojeiro & Kraljic (2022) showed via IllustrisTNG simulations and SDSS that both the gas-phase and stellar metallicities are higher for galaxies closer to filaments and nodes.

One way forward to make sense of these controversies is to use state-of-the-art galaxy formation simulations to disentangle these effects. In this context, state-of-the-art refers to simulations that reproduce the global galaxy trends in SF rate, gas content, and metallicity versus mass; restricting to such models then provides a plausible baseline for teasing out subtle environmental effects. To this end, this study explores how the scalar galaxy properties vary with respect to the distance to the closest filament identified using Discrete Persistent Structure Extractor (DISPERSE; Sousbie 2011; Sousbie, Pichon & Kawahara 2011) within the SIMBA (Davé et al. 2019) simulation suite. SIMBA reproduces many global trends related to SFR, quenched fractions, H I content, and many other global properties (e.g. Davé et al. 2019, 2020). In this first paper, we quantify trends in 3-D space (i.e. not accounting for redshift space distortions) using all resolved SIMBA galaxies to better understand the intrinsic impact of filaments on galaxy properties. We examine stellar mass (M_*), specific SFR (sSFR), H I, and H_2 fractions, metallicity, and quenched fractions versus distance to the nearest filament. We focus on galaxies outside of massive haloes ($M_h \leq 10^{13} M_\odot$) in order to restrict ourselves to a classical field galaxy sample. We study both intrinsic quantities versus distance to filament, as well as departures from the ‘main sequence’ of these quantities versus M_* in order to control for the fact that galaxies near filaments are more massive. In addition, we use SIMBA’s feedback variants to understand which trends come from LSS versus particular feedback processes (as modelled in SIMBA). Finally, we apply the same procedure to the EAGLE (Schaye et al. 2015) and IllustrisTNG (Weinberger et al. 2017; Marinacci et al. 2018; Naiman et al. 2018; Nelson et al. 2018, 2019; Pillepich et al. 2018, 2019; Springel et al. 2018) simulations to determine whether the trends seen with SIMBA are robust to variations in galaxy formation model. We leave for future work a redshift-space comparison to observations, applying observational selection and uncertainties to robustly quantify constraints on galaxy formation models.

The rest of the paper is structured as follows: Section 2 describes the tools and methods implemented in this study; Section 3 presents the trends of the galaxy properties of interest with respect to their proximity to filaments, while Section 4 investigates further the deviations of these properties from their scaling relations with M_* ,

with respect to distance from filaments; Sections 5 and 6 compare the impact of the SIMBA’s feedback variants and massive haloes, respectively, with the impact of the cosmic web; Section 7 compares our main findings with the results of the EAGLE and IllustrisTNG simulations and Section 8 provides a summary of this study.

We adopt the cosmological constants of the Planck Collaboration (Planck Collaboration XIII 2016), implemented in SIMBA: $\Omega_m = 0.3$, $\Omega_\Lambda = 0.7$, $\Omega_b = 0.048$, $H_0 = 60 \text{ km s}^{-1} \text{ Mpc}^{-1} h^{-1}$, $\sigma_8 = 0.82$, and $n_s = 0.97$.

2 SIMULATIONS AND ANALYSIS

In this section, we discuss the methods employed throughout our study in order to obtain the relevant galaxy properties and cosmic web features.

2.1 SIMBA

We use the large-scale cosmological hydrodynamical SIMBA simulations (Davé et al. 2019) for this work. SIMBA builds upon its predecessor MUFASA (Davé, Thompson & Hopkins 2016) which uses the Meshless Finite Mass version of the GIZMO code (Hopkins 2015), together with the GADGET-3 tree-particle-mesh gravity solver (Springel 2005). We refer the reader to Davé et al. (2019) for a full description and here summarize the relevant features of this work.

SIMBA models non-equilibrium cooling from primordial elements along with metal-line cooling using GRACKLE-3.1 (Smith et al. 2017), employing a spatially uniform photoionizing background attenuated with a simple prescription for self-shielding in dense regions. The chemical enrichment module makes use of yield tables for Type II supernovae (SNII, Nomoto et al. 2006), Type Ia supernovae (SNIa, Iwamoto et al. 1999), and asymptotic giant branch stars (Oppenheimer & Davé 2006). Using the metallicity and local column density, the H_2 fraction in each gas element is computed via the subgrid recipe from Krumholz & Gnedin (2011). SF then proceeds assuming a Schmidt (1959) relation law with 2 per cent of the H_2 mass being converted into stars in a local dynamical time, with a minimum density of $n_{\text{H}} > 0.13 \text{ cm}^{-3}$ for SF to occur. Galactic winds, putatively driven by SNII, are modeled in a kinetic manner, with kick probability and velocity assigned to roughly mimic scalings with galaxy stellar mass as predicted by the Feedback in Realistic Environments simulations (Muratov et al. 2015; Anglés-Alcázar et al. 2017). After the kick, a wind element does not feel hydrodynamic forces or cooling until it reaches a density 1 per cent of the threshold density for SF, or 2 per cent of a Hubble time from launch. 30 per cent of the winds are heated to the temperature provided by SNII, and winds are metal loaded by assigning a metallicity dZ to each wind particle via $dZ = f_{\text{SNII}} y_{\text{SNII}}(Z) / \text{MAX}(\eta, 1)$, where $f_{\text{SNII}} = 0.18$ is the stellar mass fraction lost to supernova, $y_{\text{SNII}}(Z)$ is the metal-dependent Type II SN yield for each species and η is the mass-loading factor. SIMBA locks individual metals into dust, removing them from the gas phase, following Li, Narayanan & Davé (2019). Taking all these aspects into consideration, SIMBA predicts mass–metallicity relation (MZR) evolution (Davé et al. 2019), and SF rate evolution (Katsianis et al. 2021) in agreement with observations, typically as well or better than other comparable simulations.

SIMBA simulates black hole growth via torque-limited accretion (Hopkins & Quataert 2011; Anglés-Alcázar, Özel & Davé 2013; Anglés-Alcázar et al. 2015) for cool gas and Bondi accretion for hot gas. Black hole feedback is modeled as a mixture of kinetic feedback and X-ray energy feedback. The kinetic mode is designed to reproduce the observed two-mode feedback, separated via the

Eddington fraction f_{Edd} . In the high-accretion mode, radiative AGN winds are modeled by assigning outflow velocities to the gas particles surrounding the black hole, dependent on the corresponding black hole mass. In the jet mode, initiated once $f_{\text{Edd}} < 0.2$ and maximized when $f_{\text{Edd}} < 0.02$, the assigned outflow velocities adopt considerably larger values than in the high-accretion modes, increasing with decreasing f_{Edd} . The X-ray feedback is introduced in a full-speed jet scenario, and when the ratio $M_{\text{gas}}/M_* < 0.2$. This involves injecting energy into the surrounding gas usually via a spherical outwards push. In SIMBA, the accretion energy determines galaxy quenching, with the jet mode feedback primarily responsible for this aspect and the X-ray feedback contributing significantly to suppressing residual SF. As a result of this AGN growth and feedback model, SIMBA reproduces the observed stellar mass function evolution from $z = 6 \rightarrow 0$, the star-forming main sequence, and quenched fractions in agreement with observations (Davé et al. 2019).

Galaxies and haloes are identified in post-processing using the CAESAR package, as described in Davé et al. (2019). During the run, particles are grouped into haloes using a 3D friends-of-friends (FoF) algorithm using a linking length of 0.2 times the mean interparticle spacing. Within each halo, CAESAR identifies galaxies using a 6D FoF with a smaller linking length, applied to cool gas and stars only. Stellar mass and SFR are computed as the total values among all particles grouped into a single galaxy (or halo). The metallicity is computed in several ways, including stellar mass-weighted (from star particles) and SFR-weighted (from gas elements). Given that considerable amounts of H I can be present in extended regions outside the star-forming regions of galaxies, CAESAR assigns each particle to the galaxy to which it is most gravitationally bound, then sums the total H I from those particles. H_2 is computed similarly, though the vast majority of H_2 lies within CAESAR galaxies. There is good agreement between the observations and the SIMBA simulated galaxy H I and H_2 fractions, as well as their scaling relations with stellar mass (Davé et al. 2020).

In this work, we focus on the $(100 \text{ comoving Mpc } h^{-1})^3$ main SIMBA run, evolved from $z = 249 \rightarrow 0$ with 1024^3 gas elements and 1024^3 dark matter particles. The minimum (adaptive) gravitational softening length for this simulation is $\epsilon_{\text{min}} = 0.5 h^{-1} \text{ kpc}$. The mass resolution for the initial gas element and dark matter particles are $m_{\text{gas}} = 1.82 \times 10^7 M_\odot$ and $m_{\text{DM}} = 9.60 \times 10^7 M_\odot$, respectively. This gives a minimum resolved stellar mass for galaxies as $M_{*, \text{min}} = 5.8 \times 10^8 M_\odot$, i.e. 32 gas/stellar element masses (star particles have, on average, same mass as gas particles, m_{gas}). We utilize the CAESAR catalog to infer the galaxy properties of interest, at redshifts $z = 0, 1, \text{ and } 2$ (i.e. snapshots 151, 105, and 78). We also use the feedback variant runs of SIMBA, which have the exact same resolution except in a $50 \text{ Mpc } h^{-1}$ box with 2×512^3 particles, and whose runs turn off individual feedback modules as we will detail later.

2.2 Tracing the cosmic web with DISPERSE

To identify filaments of the cosmic web, we use the publicly available code DISPERSE (Sousbie 2011; Sousbie, Pichon & Kawahara 2011), using the Discrete Morse theory and the theory of persistence. DISPERSE measures the gradient of the density field via Delaunay Tessellation (e.g. Schaap & van de Weygaert 2000) to identify the critical points, defined as the points where the gradient of the density field is null. Filaments are then constructed as segments connecting a maximum to a saddle point, representing the ridges of the Delaunay density field.

We applied DISPERSE to the distribution of galaxies in SIMBA, adopting a 3σ persistence threshold in order to remove the filaments

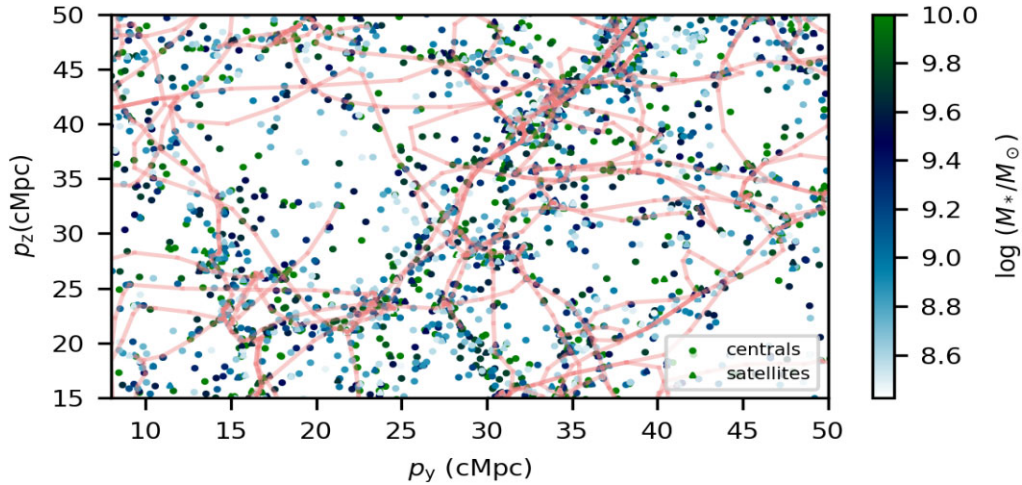


Figure 1. A 2D view of a $50 h^{-1}\text{Mpc}$ SIMBA simulation slice at redshift $z = 0$, with a slice width of $10 h^{-1}\text{Mpc}$. The galaxies are represented by circles (centrals) and triangles (satellites), colour coded by their total stellar mass. The filaments extracted from DISPERSE are plotted in pink. The figure provides a qualitative representation of the galaxies’ distribution within the cosmic web, showing that the overdensities (filaments and nodes) show predominantly massive centrals and accompanying low-mass satellites.

affected by the Poisson noise of the density distribution. As explained in, for example, Codis et al. (2018) and Kraljic, Davé & Pichon (2020), we also noted that a higher threshold would result in more robust structures with a significant drop in the number of filaments generated, hence the 3σ value adopted throughout this work represents an optimal choice. Additionally, we also applied a smoothing to the positions of the filaments’ edges, by averaging their positions with those of the edges of contiguous segments. This gives rise to a smoother filamentary skeleton by reducing unphysical filamentary shapes. These procedures generally mimic previous works that applied DISPERSE to simulations.

For better visualization, Fig. 1 shows the filaments extracted with DISPERSE and a 2D view of a SIMBA simulation at redshift $z = 0$, using a slice from the $50 h^{-1}\text{Mpc}$ box with a width of $10 h^{-1}\text{Mpc}$. The galaxies are overplotted (centrals as circles and satellites as triangles), colour-coded by their total stellar masses. This plot provides a qualitative image that the DISPERSE skeleton generally traces out the LSS that one picks out by eye. One can see further that the most massive galaxies tend to lie closer to filaments, together with their low-mass companions/satellites; this will be quantified in Sections 2.3 and 3.1.

2.3 The galaxy sample

For the purpose of this work, we quantify the galaxies’ positions in the cosmic web via the distance to the closest filament (d). DISPERSE reports the 3D positions of the filaments’ edges, which we used to compute the minimum distance between each galaxy and the corresponding closest filament mid-point. This is slightly different than the perpendicular closest distance, but negligibly so as pointed out in, for example, Tudorache et al. (2022), since each DISPERSE filament is actually comprised of a large number of small segments.

As mentioned earlier, we are specifically interested in trends versus filamentary environment within the field galaxy population. To this end, we remove all galaxies in haloes with a virial mass above $10^{13} M_{\odot}$, corresponding to removing all galaxies in structures of poor group size and larger, and only report all statistics based on the

remaining sample of galaxies. After doing so, we end up with 27 947 centrals and 13 997 satellites at $z = 0$; 18 746 centrals and 8108 satellites at $z = 1$, 13919 centrals and 4609 satellites at $z = 2$. This does not preclude some effect on galaxies from being in the vicinity of large haloes, so we are still including any effects associated with pre-processing outside of large haloes. None the less, such large haloes are fairly rare, and as one can see in Fig. 1, much of the filamentary structure is located in regions far from the most massive nodes.

We will further consider the impact of the environment on central and satellite galaxies separately. Centrals are taken to be the most massive galaxy within its halo, and with few exceptions typically lie within the inner 10–20 per cent of their halo. Satellites can be impacted by distinct physical processes such as ram pressure and tidal stripping, and although such processes have traditionally been associated with group and cluster environments, it is possible that the denser and hotter environment around filaments could also have an impact.

Fig. 2 shows the stellar mass distribution of satellites (blue dots) and central galaxies (red dots), with respect to the distance to the closest filament, for redshifts $z = 0, 1$, and 2 (upper left to right panels). Corresponding lower panels show the probability distribution of satellites (blue curve) and centrals (red). The upper mass threshold, visible most noticeably in the $z = 0$ upper left plot, comes from the aforementioned halo mass cut at $M_h < 10^{13} M_{\odot}$.

Overall, central galaxies skew to be more massive towards the filament spine. At short distances, only small satellites remain. The immediate proximity of filaments ($d \lesssim 0.1 \text{ cMpc}$) shows high-mass centrals accompanied by their respective low-mass satellites in the low-redshift Universe, while this distribution appears to be more spread out at redshift $z = 2$, indicating a dynamical evolution of the satellite population. At all redshifts, the satellites distribution peaks at $< 1 \text{ cMpc}$ from the closest filament, while for centrals the corresponding peak is at a few cMpc. This reflects the trend of the halo occupation distribution with M_* , since M_* is well correlated with M_h (e.g. Cui et al. 2021) and the halo occupancy rises quickly towards higher M_h . These galaxies represent the sample that we will use for the majority of the analysis that we discuss next.

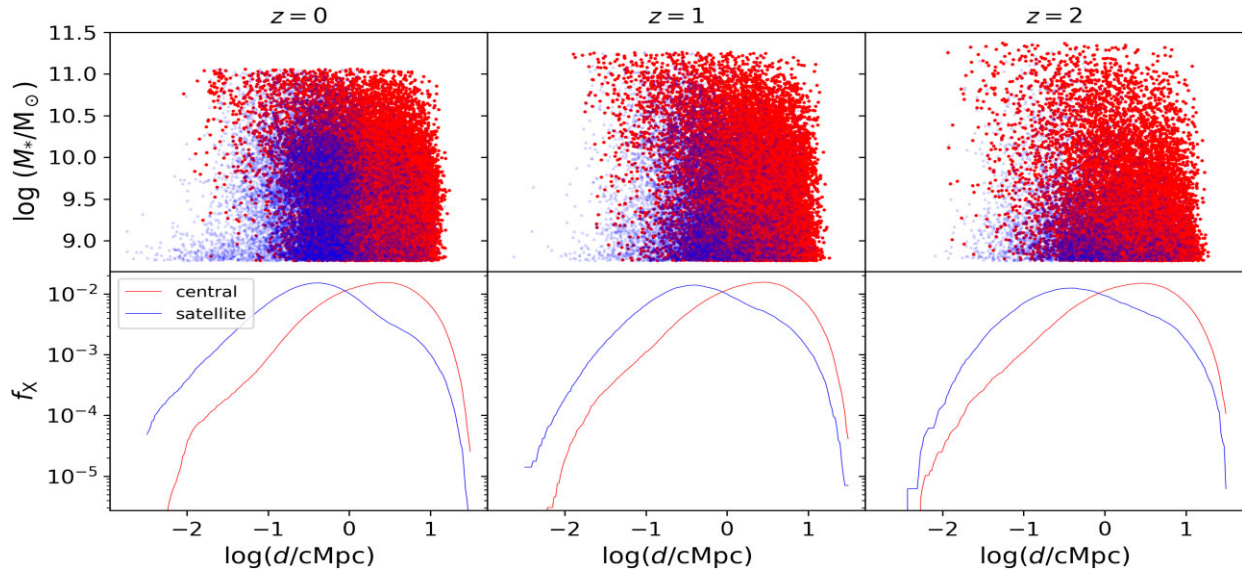


Figure 2. Upper panels show the stellar mass of satellites (blue dots) and centrals (red dots) versus the distance to their corresponding closest filament in comoving Mpc, d at redshifts $z = 0, 1,$ and 2 . Lower panels likewise present the probability distribution function of satellites (blue line) and centrals (red line) versus d . Within 1 cMpc there are fewer low-mass centrals and more satellites. The upper envelope visible especially at $z = 0$ results from our halo mass threshold of $M_h < 10^{13} M_\odot$. This figure strengthens the qualitative findings from Fig. 1, but also shows that the largest fraction of satellites and centrals are located at ~ 1 and 10 cMpc of a filament, respectively.

3 GALAXY PROPERTIES IN THE COSMIC WEB

In this section, we correlate key global galaxy properties with their proximity to filaments as measured by d . We consider each property in turn: M_* , sSFR, Z_* , f_{HI} , and f_{H_2} , where the latter two are the gas mass fractions in each phase with respect to stellar mass. We also consider quenched fractions f_Q and elliptical fractions f_e . We present results for $z = 0, 1,$ and 2 , separated into centrals and satellites.

3.1 Stellar mass

The galaxy stellar masses dependence on d is shown in Fig. 3, showing the medians of the binned values for redshifts $z = 0$ (purple), $z = 1$ (maroon), and $z = 2$ (green). Solid and dashed lines show centrals and satellites, respectively. The shaded regions represent the standard deviation on the mean in each bin, illustrating higher uncertainties in the filaments' proximity owing primarily to the lower number of galaxies in this region. We present the distance d in both comoving Mpc (left panel) and physical Mpc (right panel). We also compared the two choices for d for the other properties (presented in the following sections) and found that the trends are independent of this choice. However, the former representation offers a more visually comprehensive description of the trends and will be retained throughout this section.

At all three redshifts considered, the masses of the central galaxies decrease with increasing distance from the closest filament. Despite our finding from the previous section suggesting that at $z = 2$ galaxies adopt a broad range of masses in the filaments proximity, Fig. 3 shows that the median values of these masses are, in fact, higher for galaxies closer to the filaments. This finding can be explained via the environmental effects on the halo mass function, which predicts more massive haloes to lie closer to filaments, which then leads to higher mass galaxies in these regions (e.g. Alam et al. 2019). This highlights that we must be careful when interpreting trends with distance from filaments to ensure that they are not simply reflecting trends with stellar mass, since one of the crucial aspects of this study

is to disentangle the effects of mass and environment on galaxy properties.

The satellites curiously show a reverse trend for short distances (i.e. within $\log(d/\text{cMpc}) \lesssim -1$) at redshifts $z = 0$ and 1 , as their masses increase with distance. For larger distances, they also adopt a subtle overall decreasing trend, considerably weaker than for centrals. No clear trend is observed for satellites at redshift $z = 2$.

In agreement with our qualitative findings from Section 2.3, it appears that most massive central galaxies lie within short distances from the filaments and host a large number of low-mass satellites. This finding also supports the predictions of the environmental effects on the halo mass function, as the massive systems in the filaments to proximity are more likely to accrete more low-mass satellites. The disappearance of more massive satellites very close to filaments could further owe to dynamical effects such as accelerated dynamical friction and tidal stripping in dense environments; we defer a detailed analysis of this to future works. For now, we note this as an interesting prediction from SIMBA.

3.2 (Specific) star formation rate

Galaxies near filaments could be enhanced in SF relative to those far away since there is more gas in the vicinity, or they could be suppressed because the filaments are heated which can suppress accretion. Hence, SFR provides a key barometer for the interplay between galaxy growth and filamentary LSS. To mitigate the fact that galaxies closer to filaments have larger M_* as found in the previous section, we consider the sSFR, although the broad results are similar if we consider the SFR itself.

Fig. 4 presents the dependence of the sSFR with respect to distance from filaments at $z = 0, 1, 2$. The line styles and colours mimic Fig. 3. For all non-star forming galaxies (SFR = 0), we set $\log(\text{sSFR}) = -14$. Since we are considering medians, the analysis is not sensitive to the exact value as long as it is very low.

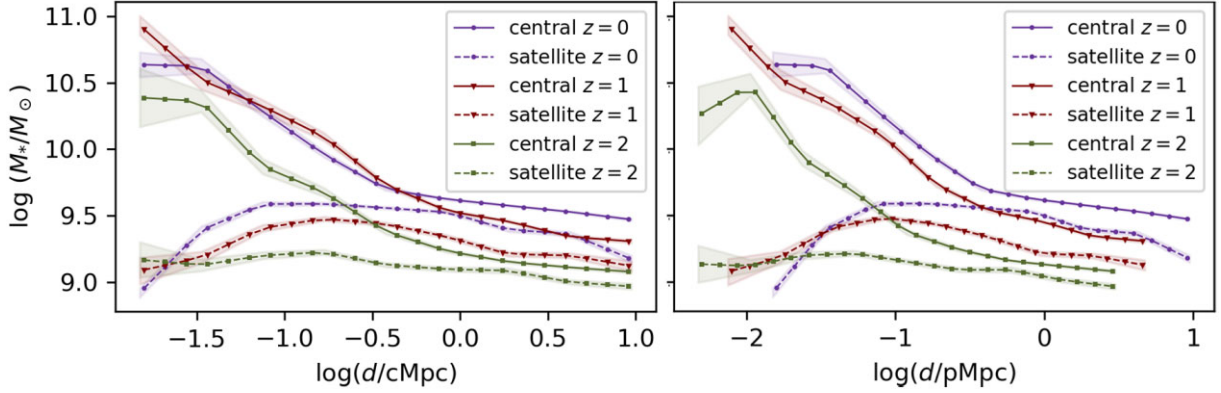


Figure 3. Distance from filaments dependence of stellar masses for centrals (continuous lines) and satellites (dashed lines) for three redshifts: $z = 0$ (purple), $z = 1$ (dark red), and $z = 2$ (green). The lines were obtained by binning the results in terms of distance and interpolating the corresponding medians (i.e. running medians). The shaded regions represent the corresponding standard errors in each bin. In agreement to our qualitative findings from Section 2.3, most massive centrals lie within short distances from the filaments and host a large number of low-mass satellites. We show the distance d in both cMpc (left panel) and pMpc (right panel), finding that the overall trends maintain regardless of the units of d .

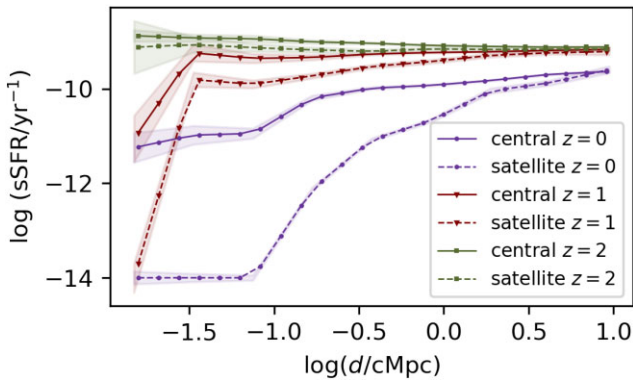


Figure 4. Distance from filaments dependence of sSFRs for centrals (continuous lines) and satellites (dashed lines) for three redshifts: $z = 0$ (purple), $z = 1$ (dark red), and $z = 2$ (green). The lines were obtained by binning the results in terms of distance and interpolating the corresponding medians (i.e. running medians). The shaded regions represent the corresponding standard errors in each bin. Galaxies close to filaments show suppressed levels of SF, with a majority of satellites in the filaments' proximity at redshift $z = 0$ being fully quenched.

As seen in Fig. 4, central galaxies clearly show a reduction in sSFR at close proximity to filaments at $z = 1$ and 0 relative to galaxies far away from filaments. At $z = 1$, the dip is only seen at very small distances ($\lesssim 30$ kpc), but by $z = 0$ the sSFR is suppressed farther out to ~ 100 kpc. At $z = 2$, if anything there is a rise in the sSFR towards filaments, perhaps indicating a reversal in the SF–density relation; we will explore this further in future work. Far away from filaments, there is an overall reduction in sSFR that reflects the global decline in cosmic SF over time (e.g. Daddi et al. 2007; Davé 2008) primarily due to falling accretion rates (Dekel et al. 2009). Hence, the growth of centrals via SF is clearly retarded even in filamentary regions, indicating evidence for pre-processing of galaxies before falling into galaxy groups or clusters.

Examining the satellites, at $z = 0$, the satellites' median sSFR vanishes within 100 kpc of filament, indicating that more than half the satellites are fully quenched. Then, the sSFR shows a rapid increase with increasing distance, converging subsequently to the same value as centrals by ~ 10 Mpc. At redshift $z = 1$, the sSFR for satellites follows that of centrals but shows somewhat more suppression

close to filaments, while becoming similar to centrals at $\gtrsim 2$ Mpc. Meanwhile, at $z = 2$, satellites show only a very mild suppression with respect to centrals. These trends indicate that satellites are more impacted by filamentary environments than centrals, albeit in a qualitatively similar way, and the additional impact grows rapidly from $\sim 1 \rightarrow 0$.

To sum up, our results show that galaxies close to filaments are suppressed in stellar growth rates out to $z \gtrsim 1$, with a majority of satellites in the filaments' proximity at redshift $z = 0$ being fully quenched. Within SIMBA, it is seen that galaxy circumgalactic and even intergalactic media are strongly impacted by AGN jet feedback (Appleby et al. 2021; Sorini et al. 2022), which thereby grows the quenched galaxy population (Davé et al. 2019). Our results here suggest that AGN feedback also may be a contributor to suppressing SFRs, particularly in satellites close to filaments, although it could also owe to increased shock heating owing to the growth of LSS. We will investigate further in Section 5 the effects of AGN feedback compared to the effects of filaments solely. We also note that the interplay between filaments and AGN feedback is a non-trivial topic, filaments potentially influencing the AGN feedback. There are works suggesting that dense environments determine a deficit of the cold gas reservoir available to trigger the AGN activity (e.g. Jaffé et al. 2015; Beyoro-Amado et al. 2021), while others suggest that the ram pressure stripping acts as a triggering mechanism for AGNs (e.g. Poggianti et al. 2017; Koulouridis, Gkini & Drigga 2024). This topic is above the scope of this study and we aim to investigate it in future work. In any case, our results clearly demonstrate that both centrals and satellites undergo pre-processing outside of galaxy groups.

3.3 Gas content

Given that the sSFR is suppressed towards filaments, one would expect that the gas contents that fuel SF would also be lowered. For molecular hydrogen, SIMBA directly ties the H_2 content to SF, but for HI, this provides a reservoir on larger scales that could be more influenced by environmental effects. Hence, it is interesting to examine the molecular and atomic contents of galaxies as a function of distance to filaments. Again, to mitigate the overall trend that the gas contents increase with mass (at least among star-forming systems), we consider the atomic and molecular Hydrogen fractions $f_{HI} \equiv M_{HI}/M_*$ and $f_{H2} \equiv M_{H2}/M_*$.

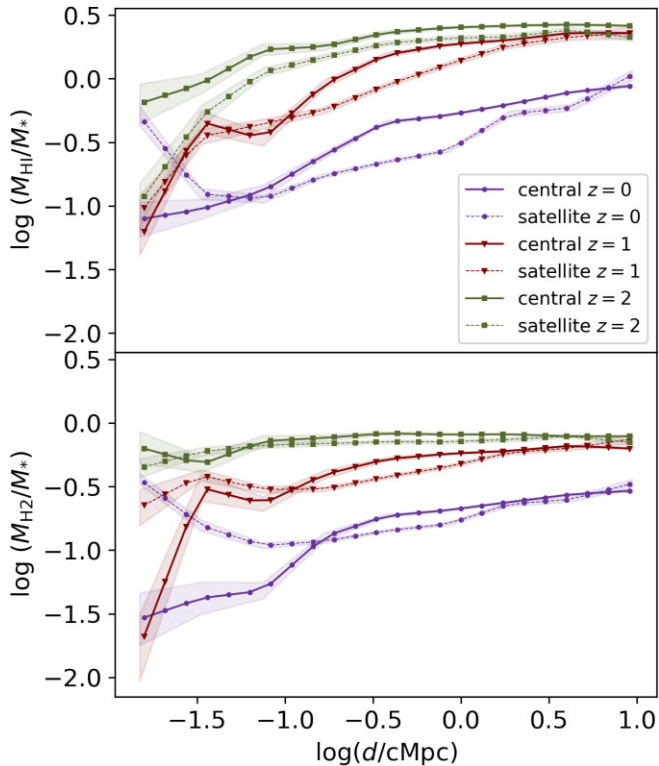


Figure 5. Distance from filaments dependence of HI (left panel) and H₂ (right panel) content for centrals (continuous lines) and satellites (dashed lines) for three redshifts: $z = 0$ (purple), $z = 1$ (dark red), and $z = 2$ (green). The lines were obtained by binning the results in terms of distance and interpolating the corresponding medians (i.e. running medians). The shaded regions represent the corresponding standard errors in each bin. The HI fraction increases with increasing distance from filaments at all three redshifts considered. $f_{\text{H}2}$ shows similar trends at redshifts $z = 0$ and $z = 1$, while (similar to sSFR, see Fig. 4) showing no clear trend for $f_{\text{H}2}$ versus distance from filament at redshift $z = 2$.

Fig. 5 shows f_{HI} (top panel) and $f_{\text{H}2}$ (bottom panel) as a function of filamentary distance, using the same colour and line type scheme as the previous plots. For central galaxies (solid lines), the trends broadly mimic that for the sSFR: Galaxies have suppressed gas contents close to filaments, with that suppression increasing in strength and extent towards lower redshifts. In detail, H₂ traces sSFR more faithfully, while HI even shows suppression near filaments even at $z = 2$, and a larger range of suppression.

The satellites, however, behave substantially differently from sSFR. At $z = 2$, there is little difference in $f_{\text{H}2}$ between centrals and satellites, but for f_{HI} the satellites show an increased suppression near filaments. However, these trends tend to reverse near filaments at lower redshifts: The satellite gas fractions are generally comparable to (at $z = 1$) or even higher ($z = 0$) near filaments versus the centrals. This is an odd turn, which may have to do with the way that the gas fractions are computed by including all gas within haloes that is most bound to a given galaxy. In galaxy groups, it has been observed that HI can be present throughout the group environment (e.g. Lucero et al. 2015), and in our HI assignment scheme that gas may have been associated with group satellites. If the same effect is happening in the densest regions of filaments, this HI may in detail not be associated with individual galaxies, but rather the overall environment. It is less easy to understand the upturn in $f_{\text{H}2}$ at a low distance. This could partially be explained by the HI association for satellites, but

in order to disentangle these effects and make proper predictions for comparison to data we would need to create mock data cubes of these systems (as in Glowacki, Elson & Davé 2021), which is beyond the scope here.

Overall, the galaxies do not seem to show as much suppression in gas content as in sSFR (more visible for satellites). Since sSFR can be decomposed into $f_{\text{H}2}$ times the SF efficiency ($\text{SFE} \equiv M_{\text{H}2}/M_*$), this suggests that there are variations in the efficiency of converting gas into stars, with the SFE generally being lower closer to filaments.

In summary, our results show that the HI fraction increases with increasing distance from filaments at all three redshifts considered, with satellites at redshift $z = 0$ showing an initial decrease in gas fractions near filaments. $f_{\text{H}2}$ shows similar trends at redshifts $z = 0$ and $z = 1$, while (like sSFR) showing no clear trend for $f_{\text{H}2}$ versus distance from filament at redshift $z = 2$. The satellites show a curious increase in gas fractions at $z \leq 1$ very close to filaments, which may owe to analysis methodology, and highlights the difficulty of unambiguously assigning particularly HI to galaxies in dense environments.

3.4 Metallicity

Another key global galaxy property is its metallicity. Galaxies are known to have a strong correlation of M_* with Z known as the MZR (e.g. Trager et al. 2000; Tremonti et al. 2004; Maiolino & Mannucci 2019). This is believed to be set by a competition between pristine inflow diluting metallicity, SF enhancing metallicity, outflows removing metals, and the re-accretion of outflows providing an additional source of metals (e.g. Finlator & Davé 2008; Davé, Finlator & Oppenheimer 2012). Particularly, the latter effect could be impacted by environment, because the gas in denser regions may be more enriched from previous star formation activity and may retard outflows leading to more re-accretion. For satellites in denser regions, one expects there to be less pristine inflow and more enriched recycling, leading to higher metallicities; indeed, this is found in simulations (e.g. Davé, Finlator & Oppenheimer 2011). These trends are for the gas-phase metallicity, but models generally predict the stellar metallicity traces this reasonably well. Here, because we want to compare across both gas-rich and gas-poor galaxies, we will employ the stellar metallicity (Z_*) versus filamentary distance since this can be computed for all galaxies.

Fig. 6 shows the median $Z_*(d)$, using the same colour and line scheme as in previous plots. In all cases, the metallicities are overall higher in the filaments proximity. Given the MZR, or even the fundamental metallicity relation (FMR, Mannucci et al. 2010), our results can be explained via the higher mass and low SFR galaxies present in the filaments' proximity.

The centrals show an abrupt drop in metallicity when moving away from filaments, and the differences between centrals and satellites, in this case, are less obvious compared to the previous quantities (Section 3.2). In general, the satellites have slightly lower metallicity, but this is likely most explained by their lower M_* . However, when comparing to Fig. 3 and considering the MZR, this similarity between centrals and satellites is actually somewhat surprising. This is because the satellites' median M_* 's are quite flat with distance, yet their metallicity continues to increase strongly towards filaments just like the centrals. This indicates that there is a strong effect from the suppression of SFR (i.e. the FMR), and perhaps also an effect from the environment.

Additionally, the trends observed appear to be weaker at low redshift. A possible explanation for this might be the steeper mass–metallicity correlation observed in SIMBA at high redshift, $z \sim 2$

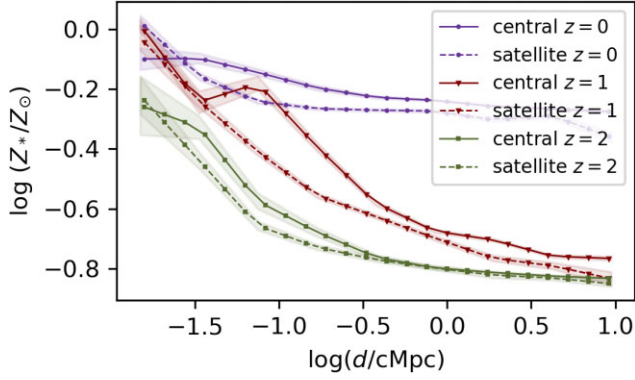


Figure 6. Distance from filaments dependence of stellar metallicities for centrals (continuous lines) and satellites (dashed lines) for three redshifts: $z = 0$ (purple), $z = 1$ (dark red), and $z = 2$ (green). The lines were obtained by binning the results in terms of distance and interpolating the corresponding medians (i.e. running medians). The shaded regions represent the corresponding standard errors in each bin. Galaxies close to filaments are more metal-enriched, the centrals and satellites showing similar behaviours.

(see Davé et al. 2019). However, the change is quite dramatic from $z = 1 \rightarrow 0$, with galaxies far from filaments being much more enriched at late times. This suggests another effect, such as wind recycling of enriched materials even far from filaments, being more important since $z \sim 1$. We plan to investigate the detailed evolution of metallicity as a function of environment in future work.

In short, our results show that galaxies close to filaments are more metal-enriched, the centrals and satellites showing similar behaviours. The trend with the satellites, combined with the lack of a trend in M_* in contrast with the dramatic evolution in satellites’ SFR, suggests that the FMR is an important driver in setting the environmental trends. The trend substantially weakens by $z = 0$, owing to some complex interplay between the environment and the various physical processes governing galaxy metallicities.

3.5 Quenching and morphology

We have seen that galaxies, and satellites in particular, have lower sSFRs near filaments at $z \lesssim 1$. Another way to quantify this is using the quenched fraction f_Q , which we compute via the Williams et al. (2009) UVJ diagram. Quenching is also well-known to be correlated with morphology. Hence, we also examine the elliptical fraction f_e , which we define using the fraction of kinetic energy in rotation (Sales et al. 2012) since Kraljic, Davé & Pichon (2020) found that this was the most well-correlated measure reflecting visual morphology in SIMBA. We chose a threshold of 0.3, meaning that galaxies with a smaller fraction of kinetic energy in rotation are considered elliptical, but varying this from 0.25 or 0.35 does not affect the results significantly.

Fig. 7 shows the galaxies’ quenched fraction (f_Q , top panel) and elliptical fraction (f_e , bottom panel) as a function of distance from filament, using the same scheme as in previous plots. We note that the distance range adopted for this analysis is smaller than in the previous cases. This is because at large enough distances from filaments ($\log(d/cMpc) \gtrsim 0.5$) the corresponding behaviours are reasonably well converged.

As expected from Section 3.2, both centrals and satellites are more quenched close to filaments. A decreasing trend is not visible at redshift $z = 2$, but becomes prominent at $z \leq 1$. The quenched

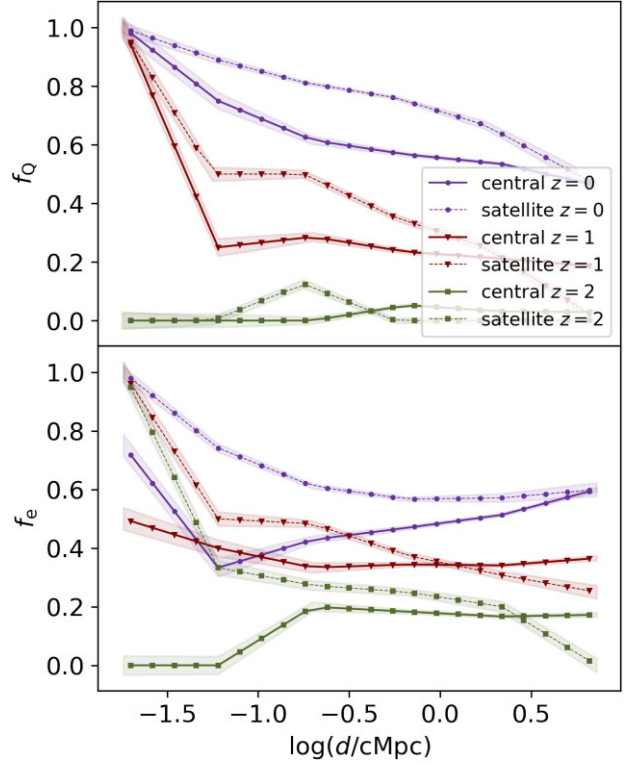


Figure 7. Distance from filaments dependence of quenched fractions (left panel) and elliptical fractions (right panel) for centrals (continuous lines) and satellites (dashed lines) for three redshifts: $z = 0$ (purple), $z = 1$ (dark red), and $z = 2$ (green). The lines were obtained by binning the results in terms of distance and interpolating the corresponding medians (i.e. running medians). Galaxies close to filaments are more elliptical and quenched at low redshift, the trends being more prominent for satellites.

fraction increases with time, which follows the trend seen in the overall galaxy population in SIMBA, as well as in observations.

The trend is similar for both centrals and satellites, but the satellites have a higher overall f_Q . Within $\lesssim 100$ ckpc of filaments at $z = 0$, ~ 90 per cent of satellites are quenched, as opposed to ~ 70 per cent of centrals. This shows again the important role that the environment plays in quenched satellite galaxies, which is already prominent around filamentary structures. At $z = 2$, however, little difference is seen between the central and satellite quenched fractions. Hence, the environmental effects are restricted to lower redshifts, where LSS causes more shock heating and AGN feedback provides significant energy into the IGM in SIMBA. These findings echo our results from Section 3.2, quantified in a different way that provides another testable prediction from SIMBA.

In general, f_e increases with time, and the satellites’ f_e are higher than that of the centrals, with the difference between them also growing with time. However, the elliptical fraction as defined here shows overall less evolution than the quenched fractions, and particularly at $z \leq 1$ the elliptical fractions for centrals very close to filaments show no evolution. At large distances, centrals and satellites show similar elliptical fractions. In general, it is more difficult to compare our elliptical fractions defined via κ_{rot} to observations since this is not so easy to measure, but this at least qualitatively demonstrates that, in general, SIMBA galaxies become less rotationally supported with time and proximity to filament.

To sum up, our results show that galaxies close to filaments are more elliptical and quenched, the trends being more prominent for

satellites. For both centrals and satellites, the quenched fraction is similar at redshift $z = 2$, although the elliptical fractions are still a bit higher for satellites at $z = 2$. The higher elliptical fraction suggests galaxies that are likely to be more massive, passive, and metal-enriched, with lower gas content, tend to have less rotational support, concordant with the results noticed in previous sections (Section 3.1–3.4). The fact that f_e and f_Q do not mimic each other exactly even qualitatively in their trends with d and redshift suggests that quenching and morphological transformation are not happening in exactly the same galaxies at the same time within SIMBA. However, the crudeness of the morphological measure begs further investigation to disentangle the relation between quenching and morphology, perhaps requiring higher resolution simulations capable of resolving the scale height of typical disks.

4 DEVIATIONS FROM THE SCALING RELATIONS

We have seen that proximity to DISPERSE-identified filaments has the effect of lowering SF and gas content, raising the metallicity, and increasing the elliptical fraction of galaxies at $z \lesssim 1$, effects that are enhanced amongst satellite galaxies. However, these effects with d are qualitatively degenerate with stellar mass – that is, galaxies with higher mass which tend to be found closer to filaments also share these general trends. Thus it is important to examine whether the effects are truly due to the location in the cosmic web.

To do this, as mentioned earlier, in this section, we investigate many of the same quantities and their trends with d , but now at fixed stellar mass M_* . For this purpose, we compute the deviations of the quantities of interest from their scaling relations with stellar mass, specifically the star formation main sequence (SFMS), MZR, and the HI and H₂ fractions relations with M_* . By comparing these to the corresponding ones in the previous section, we can see how much of the effect owes to its stellar mass dependence and how much owes to the impact of filamentary LSS.

4.1 Deviation from star-forming main sequence

The (specific) SF rate is expected to have a clear dependence on mass via the SFMS (see e.g. Noeske et al. 2007), which, as mentioned in Section 2.1, is reasonably reproduced in SIMBA. We obtain the SFMS by fitting the medians of sSFR in bins of M_* for all star-forming galaxies defined as $\log(\text{sSFR}/\text{yr}^{-1}) > -10.8 + 0.3z$, same as in Davé et al. (2019). We have kept our definition of star-forming galaxies simple despite there being more sophisticated ways to define the SFMS (see e.g. Hahn et al. 2019) in order to be more straightforwardly comparable with observations in the future. For instance, changing the $z = 0$ threshold from $-10.5 \rightarrow -11$ has little effect on the results, since we are only concerned with the relative deviation of galaxies near filaments versus those of the overall galaxy population.

Fig. 8 shows the deviation from the SFMS ($\Delta \log$ sSFR) as a function of d at $z = 0, 1, 2$, for centrals (solid) and satellites (dashed). This can be compared to Fig. 4, which shows the corresponding plot for sSFR itself.

Overall, the trends look qualitatively, and for the most part quantitatively, similar to those for sSFR: the centrals show an increasing suppression of SF activity with time very close to filament centres, with no strong trend at $z = 2$ while by $z = 0$ the typical galaxy at the centre of a filament is quenched. The satellites likewise show a strong trend with redshift, with suppression of SF activity extending to quite large distances by $z = 0$. This indicates that the effects in

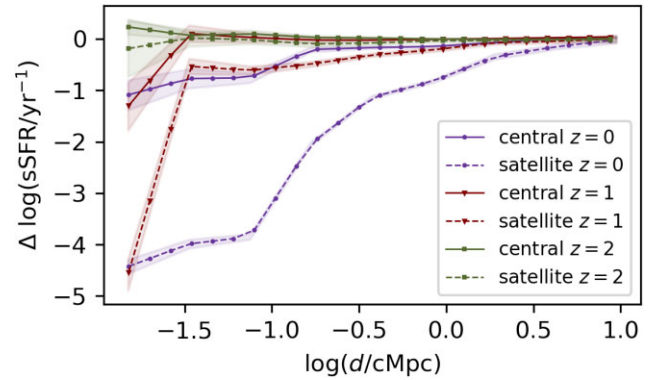


Figure 8. Distance from filaments dependence of the sSFRs’ deviations from the SFMS for centrals (continuous lines) and satellites (dashed lines) for three redshifts: $z = 0$ (purple), $z = 1$ (dark red), and $z = 2$ (green). The lines were obtained by binning the results in terms of distance and interpolating the corresponding medians (i.e. running medians). The shaded regions represent the corresponding standard errors in each bin. The centrals show an increasing suppression of SF activity with time very close to filament centres, with no strong trend at $z = 2$ while by $z = 0$ the typical galaxy at the centre of a filament is quenched. The satellites likewise show a strong trend with redshift, with suppression of SF activity extending to quite large distances by $z = 0$ (see also Fig. 4).

sSFR seen previously do not owe primarily to any mass dependence in galaxies as a function of d .

In detail, the trends in $\Delta \log$ sSFR are slightly weaker than those seen in sSFR. For instance, at $z = 0$, the central galaxies close to filaments lie ~ 1 dex below those at $z = 2$ in $\Delta \log$ sSFR, while in Fig. 4 the difference is closer to ~ 2 dex. But much of that difference is explained by the fact that sSFRs at $z = 2$ are generally higher than at $z = 0$. We conclude that the trends in M_* as a function of d are not an important factor in establishing the suppression of SF activity near filaments and that such effects genuinely owe to environmental effects from the cosmic web.

4.2 Distance from HI and H₂ mean relations

The HI and H₂ fractions are known to have a clear dependence on galaxy stellar mass (e.g. Obreschkow & Rawlings 2009; Catinella et al. 2010; Maddox et al. 2015). SIMBA reproduces these trends fairly well, as shown in Davé et al. (2020). We obtain the underlying scaling relations by fitting a running median of each gas fraction as a function of M_* . This then allows us to compute the corresponding deviations $\Delta \log(M_{\text{HI}}/M_*)$ and $\Delta \log(M_{\text{H}_2}/M_*)$.

Fig. 9 shows these quantities Δf_{HI} and Δf_{H_2} as a function of distance from filament d , at $z = 0, 1$, and 2 for centrals and satellites. This plot can be compared to Fig. 5, which uses the same line style scheme.

Unlike Δ sSFR discussed in the previous section, there are noticeable differences between Δf_{HI} and Δf_{H_2} versus d and the corresponding trends in the gas fractions themselves. For central galaxies, f_{HI} and f_{H_2} both show clear declines towards filaments, but the declines are much weaker or absent when considering Δf_{HI} and Δf_{H_2} . Indeed, at $z = 2$, the gas fractions at a given M_* are actually enhanced close to filaments, and this remains true for HI even at $z = 0$. At $z = 1$, there is an odd feature, present in both gas fractions as well as the sSFR, which is difficult to explain and may owe to small number statistics. That aside, it appears that at high redshifts, the filamentary LSS brings in more cool gas to supply galaxies, rather than suppressing it via shock heating. Overall, the central galaxies do

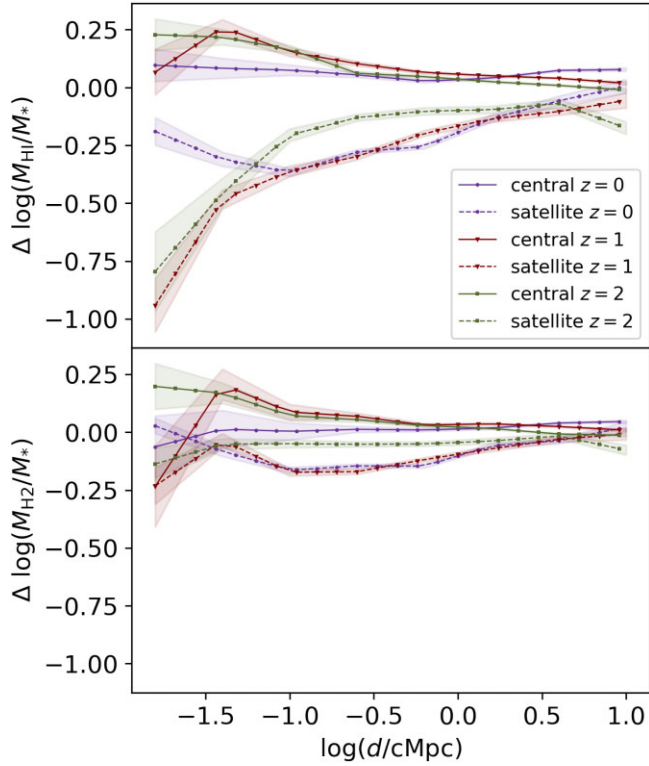


Figure 9. Distance from filaments dependence of the H I (left panel) and H₂ (right panel) fractions' deviations from the corresponding scaling relations with mass, for centrals (continuous lines) and satellites (dashed lines) for three redshifts: $z = 0$ (purple), $z = 1$ (dark red), and $z = 2$ (green). The lines were obtained by binning the results in terms of distance and interpolating the corresponding medians (i.e. running medians). The shaded regions represent the corresponding standard errors in each bin. Satellites are depleted in H I at a given M_* near to filaments at all three redshifts considered, $z = 0, 1, \text{ and } 2$, while f_{H_2} at a given M_* is not significantly depleted.

not show any significant suppression of gas contents near filaments. We also note here that the trends for centrals are flatter than for satellites and also compared to the trends found in the previous section when looking at the deviations from the SFMS (Fig. 8). However, even though the deviations here are relatively small, they are statistically significant, as illustrated by the shaded regions.

For satellites, Δf_{HI} shows significant suppression towards filaments, following similar trends for f_{HI} , including the upturn in H I content close to filaments at $z = 0$. This indicates that for H I, the mass dependence of satellites is not critical in establishing trends of gas fractions with d .

In contrast, satellites show decidedly less amounts of suppression in Δf_{H_2} close to filaments than f_{H_2} . This is particularly surprising since sSFR and ΔsSFR both show significant suppression, and the H₂ content is directly responsible for feeding SF. This shows that the molecular gas fractions have a stronger M_* dependence which yields more significant trends with d in f_{H_2} than in Δf_{H_2} . Combined with the variations in SF efficiency discussed in Section 3.3, this leads to a lack of a strong trend in $\Delta f_{\text{H}_2}(d)$.

To sum up, we can state that satellites are depleted in H I, relative to centrals, at a given M_* near to filaments at all three redshifts considered, $z = 0, 1, \text{ and } 2$. In contrast, f_{H_2} at a given M_* is not significantly depleted. Meanwhile, centrals show only weak trends, with a hint of an enhanced gas content close to filaments particularly at higher redshifts. With respect to quenching, it can be seen that

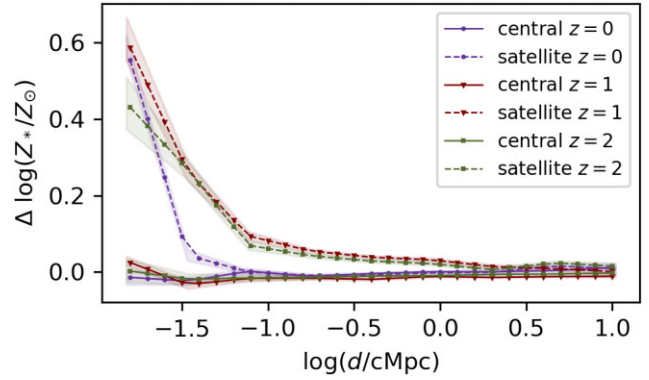


Figure 10. Distance from satellites dependence of the stellar metallicities' deviations from the MZR for centrals (continuous lines) and satellites (dashed lines) for three redshifts: $z = 0$ (purple), $z = 1$ (dark red), and $z = 2$ (green). The lines were obtained by binning the results in terms of distance and interpolating the corresponding medians (i.e. running medians). The shaded regions represent the corresponding standard errors in each bin. Satellites close to filaments show significantly higher metallicities than the MZR expectations.

the gas depletion for satellites starts at higher redshifts than the SF suppression (Section 4.1), in agreement with the recent results of Hasan et al. (2023). This may be expected as gas removal does not immediately result in reduced SF, hence we expect the gas depletion to start at earlier epochs.

4.3 Deviations from mass–metallicity relation

We likewise investigate the deviations from the MZR. As mentioned in Section 2.1, the MZR in SIMBA is seen to be in good agreement with observational results at all three redshifts considered in this study. We compute the MZR by fitting a running median for the mass–metallicity distribution of all the galaxies considered (both centrals and satellites), and then we compute the deviation ΔMZR from this fit for each galaxy, interpolated to its M_* . As previously discussed in Section 3.4, we examine the mass-weighted stellar metallicity here.

Fig. 10 shows ΔZ_* with respect to the distance from filaments d . This can be compared to the plot of $Z_*(d)$ shown in Fig. 15, which employs the same colour scheme.

The trends in $\Delta Z_*(d)$ are noticeably different than for $Z_*(d)$. Most obviously, centrals show essentially no trend of ΔZ_* with d at any redshift, whereas there was a strong trend of metallicity increasing closer to filaments. The implication is that the trend seen in the MZR owes entirely to the fact that more massive centrals live closer to filaments, and intrinsically there is no effect of centrals' metallicity caused by LSS. Given that the sSFR is significantly impacted, the implication is that the FMR (Mannucci et al. 2010) is in SIMBA predicted to be dependent on location within the cosmic web. We aim to explore a comparison of this prediction to observations in future work.

The satellites, in contrast, continue to show a significant dependency of metallicity with d at all redshifts. None the less, one sees significant differences comparing the trends in the dashed lines in Fig. 6 versus Fig. 10. For instance, at $z = 0$, $Z_*(d)$ shows a very flat dependence, while $\Delta Z_*(d)$ shows essentially no deviation until reaching very close to the filament centre, and then a strong upturn. The trends at $z = 1, 2$ are more similar between these two quantities in terms of the trend, although the overall evolution of the MZR is removed by considering ΔZ_* .

To sum up, our results show that only satellites are more metal-enriched than the MZR predictions in filaments' proximity, at all redshifts considered. A plausible explanation relies on the FMR, given the low levels of SF at fixed stellar mass for satellites close to filaments (Section 4.1). We note, however, that satellites do not show evidence of strong SF suppression at redshift $z = 2$, which again suggests that the FMR is not invariant with the environment. We speculate that this finding might be caused by the early chemical enrichment expected to primarily influence satellites in dense regions, as reported in, for example, Bahé et al. (2017) and Urban et al. (2017). Meanwhile, centrals at a given M_* show no enhancement close to filaments.

Overall, for redshift $z = 0$ and 1, we have seen that there is a significant effect on many galaxy properties close to filaments, with the effects being much stronger for satellite galaxies than for centrals. Close to filaments, galaxies (particularly satellites) tend to be less star-forming, less gas-rich, more metal-rich and are more likely to be quenched and dispersion-dominated. In detail, the suppression in gas content (and particularly f_{H_2}) is not as strong as seen for sSFR, and the stellar metallicities are not impacted by location in the cosmic web once the mass dependence of the MZR is taken out. These predictions provide a comprehensive view of the growing impact of filaments on galaxies, which could potentially be compared to observations.

5 SIMBA FEEDBACK VARIANTS

In the next two sections, we investigate the underlying cause(s) of why galaxies near filaments have systematically different properties. We focus on the suppression of SF since this is the clearest trend, and is correlated with the trends in other properties. As discussed earlier, two possibilities for why the sSFR is lower near filaments are that it owes to shock heating from LSS, or feedback heating from either SF or AGN. In particular, AGN feedback is circumstantially implicated because the environmental effects become strong at $z \lesssim 2$ and particularly at $z \lesssim 1$, which matches up with the era in which AGN feedback increasingly quenches galaxies.

With the SIMBA suite, we have an opportunity to directly test the impact of feedback mechanisms on galaxy properties in the cosmic web using the feedback variant runs. In this section, we investigate the SF properties of central and satellites at redshift $z = 0$, in the case when individual feedback modes of SIMBA are turned off as described by Section 2.1. These runs, done in a $(50 h^{-1} \text{Mpc})^3$ volume with otherwise the same resolution and input physics as the main $(100 h^{-1} \text{Mpc})^3$ volume run, exclude feedback modes one at a time.

The main motivation behind this analysis is, on the one hand, to gain a better understanding of the main causes of quenching found in Sections 3.2 and 4.1, but also to separate the potential cosmic web effects from the feedback ones. As explained in Section 4, we chose to present the results here as deviations from their corresponding scaling relations with stellar mass, in order to minimize the mass effects on our findings. We computed the SFMS for each feedback variant and then calculated the corresponding deviations. The SFMS is dependent on feedback, given that all the various feedback channels implemented in SIMBA can suppress the SF. For a more detailed description of these effects, we direct the reader to Davé et al. (2019).

Fig. 11 presents the deviations from the SF main sequence with respect to distance from filaments, when feedback is excluded (green lines) with the previous results from Section 4.1 (Fig. 8) overplotted for reference (purple lines). As before, the satellites are represented by dashed lines and centrals by solid lines. It can be seen that when feedback is not included, SF suppression is still evident in the filaments' proximity, this effect being stronger for satellites.

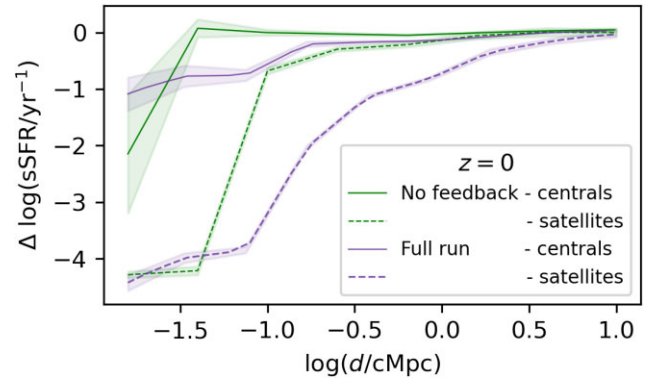


Figure 11. Distance from filaments dependence of the sSFRs' deviations from the SFMS for centrals (continuous lines) and satellites (dashed lines) at redshift $z = 0$. The green lines represent no feedback scenarios, while the purple lines resulted from the full SIMBA runs (same as the purple lines in Fig. 8). The lines were obtained by binning the results in terms of distance and interpolating the corresponding medians (i.e. running medians). The shaded regions represent the corresponding standard errors in each bin. Galaxies have sSFR suppressed near filaments even when feedback is excluded, suggesting that LSS heating is the dominant primary of the suppression.

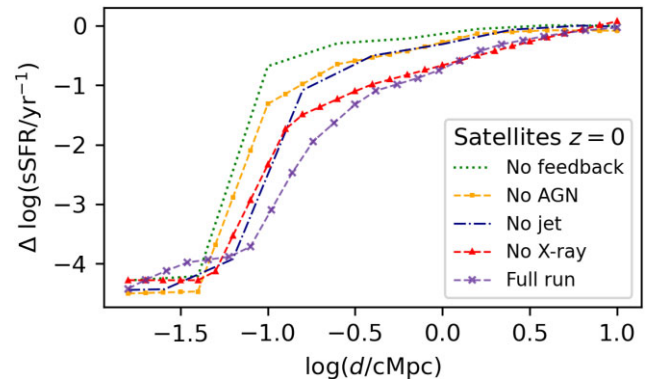


Figure 12. Distance from filaments dependence of the sSFRs' deviations from the SFMS for and satellites at redshift $z = 0$, in different feedback scenarios: no feedback (green lines) – same as in Fig. 11; no AGN (yellow lines); no jet (blue lines); no X-ray feedback (red lines); and full run (purple lines) – same as in Figs 8 and 11. The lines were obtained by binning the results in terms of distance and interpolating the corresponding medians (i.e. running medians). Note that no errors are plotted, due to the lines being very close to each other, but the approximate size of the errors in these determinations can be inferred from Fig. 11. Among feedback processes, AGN feedback has the most significant impact on providing extra suppression of sSFR near filaments.

In order to gain a better understanding of how/where feedback impacts SF, Fig. 12 shows the deviations from the SFMS for satellites at redshift $z = 0$ in different feedback scenarios. Note that no errors are shown in this plot, due to how close the lines are, but the approximate size of the errors in these determinations can be inferred from Fig. 11. It can be seen that in all cases, SF is suppressed for a broader range of distances when some feedback is included, with AGN feedback having the stronger contribution in the filaments' proximity.

It is worth mentioning that when feedback is excluded, the distance range for which SF is suppressed is shorter than in the full run/partial feedback cases, as only galaxies in the immediate proximity of filaments (i.e. $\log(d/c\text{Mpc}) \lesssim -1.4$) show evidence of SF suppression. This finding shows that feedback effects play indeed

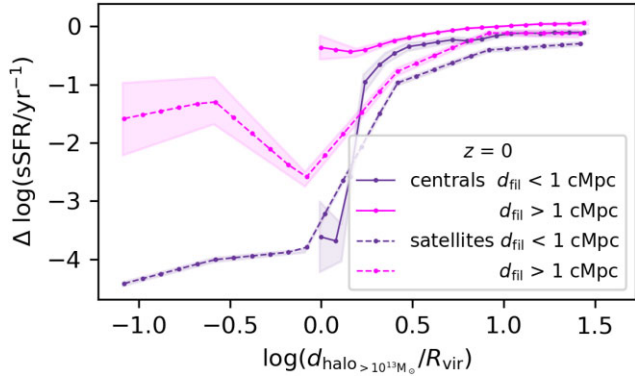


Figure 13. The deviations of the sSFR from the SFMS dependence on the distance to the closest massive halo ($M_h > 10^{13} M_\odot$) for centrals (continuous lines) and satellites (dashed lines), at redshift $z = 0$. The galaxies outside filaments ($d > 1$ cMpc) are considered separately, represented by the magenta lines. In addition to the halo effects, filamentary environments also play a non-negligible role in sSFR suppression.

a role in quenching, however, for galaxies close to filaments we need a different explanation for the suppressed levels of SF.

6 THE COSMIC WEB AROUND MASSIVE HALOES

As explained in Section 3, we have only studied galaxies within non-group haloes ($M_h \leq 10^{13} M_\odot$) in order to avoid the influence of massive haloes on the galaxy properties in the resulting cosmic web. However, the mass and spatial range over which massive haloes influence surrounding galaxies remains uncertain. For instance, Gabor & Davé (2015) showed that galaxies can undergo ‘neighbourhood quenching’ out to several virial radii, owing to elongated satellite orbits or being within the shock-heated region around a massive halo that can extend beyond the halo virial radius for quite massive systems.

Similarly, Bahé et al. (2012) and Wetzel, Tinker & Conroy (2012) investigated how the haloes’ effects on quenching vary with distance, finding a non-trivial connection. Specifically, Bahé et al. (2012) found that confinement pressure by the intracluster medium can lead to an increase in the mass of hot gas, hence galaxy quenching being a competition between ram-pressure stripping and confinement pressure. Wetzel, Tinker & Conroy (2012) also found that haloes can quench galaxies even outside the virial radius, this effect fading out at \sim two virial radii. Overall, the effects haloes have on galaxy quenching are complex and still a debated topic in the literature (e.g. Schawinski et al. 2014; Zolotov et al. 2015; Behroozi et al. 2019).

In this section, we aim to explore how massive haloes impact their surroundings in relation to the cosmic web. Specifically, we investigate further the quenching trend found near filaments in the previous sections (Sections 3.2 and 4.1), contrasted versus the influence of simply being near a massive halo regardless of the relation to a filament. Certainly, we expect the massive halo to be the dominant environmental influence in its vicinity, however, we would like to determine if there is an additional influence from being close to a filament near the massive halo.

6.1 Star formation near massive haloes

Fig. 13 shows how the deviations of the sSFR from the SFMS for the galaxies in our sample varies with the distance from the closest

massive halo ($M_h > 10^{13} M_\odot$), normalized by the virial radius R_{vir} of each corresponding closest massive halo, at $z = 0$. We define the virial radius as enclosing 200 times the critical density. We note that satellites can be found within distances as small as $\sim 0.1 R_{\text{vir}}$ of a massive halo. This happens for satellites located within the outskirts of their host halo and in the neighborhood of a massive halo. This is not the case for centrals, since they are located at the centre of their host haloes. In the purple lines, we show the results for the centrals (solid) and satellites (dashed) within 1 cMpc of a filament. In the magenta lines, we show those galaxies selected to be away from filaments, at a distance of at least 1 cMpc of a filament. Changing this threshold value does not qualitatively change the results, but lowering it makes the curves noisier due to the small number statistics while raising it lessens the effect. The fraction of all galaxies within 1 cMpc of a filament is 46.24 per cent.

Fig. 13 shows, as expected, that the sSFR is suppressed in the proximity of massive haloes, more so for satellites than centrals. Centrals converge towards the global SFMS beyond a few R_{vir} from massive haloes, showing that galaxies’ SF is impacted even outside the virial radius, though modestly so. For satellites, the impact is more dramatic, and clearly extends out to $\sim 2 R_{\text{vir}}$.

A curious feature seen in the centrals close to filaments is that the sSFR does not monotonically deviate from the global main sequence when going close to the halo centre. Instead, the deviation from the sSFR lessens at small radii. On the one hand, these galaxies are more quenched; hence, their sSFR is lower compared to the other centrals in the sample. On top of this, they are also more massive because massive galaxies tend to cluster around the most massive haloes, due to the stellar-to-halo mass relation (SFMR, see e.g. Moster et al. 2010; Girelli et al. 2020). Hence, the centrals close to filaments and also close to the centre of a massive halo ($\sim 1 R_{\text{vir}}$ from the massive halo’s centre) tend to lie significantly below the SFMS. It is also true that the small-number statistics can influence our results, but none the less the overall trend is consistent within the standard error.

Comparing between the galaxies 1 cMpc within/outside of filaments, we see that the broad trends are similar whether close to filaments or not. Hence, the dominant environmental effect around massive haloes is set by proximity to the halo. However, there are noticeable differences. For instance, central galaxies outside filaments remain close to the global sSFR well within haloes, while those within 1 cMpc of a filament are suppressed in SFR. It appears that being in a filament may initially shield a galaxy from the environmental effects of shock-heated gas generated by the massive halo, but eventually ends up seeing an increased suppression in sSFR from being near a filament. Meanwhile, satellites show a modest but distinct effect, in that being near a filament causes a cessation of SF at a slightly larger radius.

We conclude that the location within the cosmic web has a non-negligible albeit sub-dominant effect on SF in galaxies around massive haloes. While in general SF is increasingly suppressed closer to big haloes, filaments appear to play a role too, suppressing SF further in their vicinity. For satellites near filaments, the effects around central galaxies extend slightly further out as compared to satellites not near filaments. These subtle environmental trends provide interesting directions for future work to both see if this is detectable in observations and to compare to other models.

7 COMPARISONS WITH EAGLE AND TNG

State-of-the-art cosmological simulations today tend to do a good job reproducing the stellar contents of galaxies, often because they

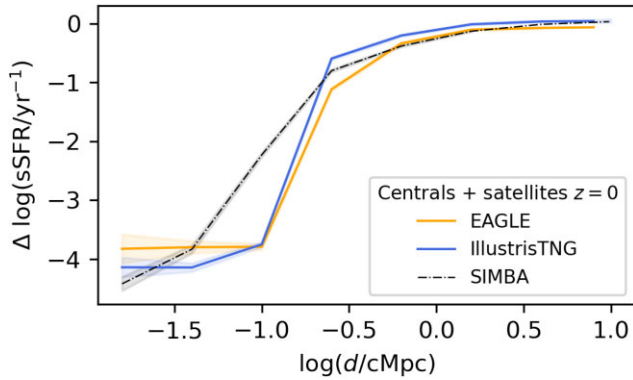


Figure 14. Distance from filaments dependence of the sSFRs' deviations from the SFMS for all galaxies computed in EAGLE (orange line) and IllustrisTNG (blue line). The lines were obtained by binning the results in terms of distance and interpolating the corresponding medians. All the determinations are made for redshift $z = 0$. sSFR is significantly suppressed near filaments in all models, with a broad agreement between EAGLE, IllustrisTNG, and SIMBA, modulo differences at $d \sim 100$ kpc.

are tuned to match the global stellar mass function. However, different models achieve this agreement using very different feedback prescriptions, which could have differing effects on galaxy sub-populations. In this section, we compare our main findings with EAGLE and ILLUSTRISTNG simulations, to assess how different their predictions are in terms of galaxies around filaments, towards potentially using this as a way to discriminate between models. Both EAGLE and ILLUSTRISTNG show similar stellar mass functions and SFMS (see fig. 2 in Davé et al. 2020). We also investigated the M_* dependence on d and found that the overall trend agrees between the three simulation suites – i.e. the stellar masses decrease when moving away from filaments. However, due to the different satellites/centrals prescriptions in the three simulation suites, we cannot draw definite conclusions regarding the differences between their stellar mass distributions around filaments and limit at saying that the overall trend agrees between the three simulations. We focus on the deviations from the SFMS and MZR, as these are the quantities publicly available for both these models, and are expected to provide reliable results, given that they incorporate the mass effects. The subsequent plots in this section show the combined trends of centrals and satellites (i.e. we do not distinguish between them).

For both EAGLE and ILLUSTRISTNG, we identified filaments by applying DISPERSE to their galaxy catalogs exactly as described in Section 2.2. Additionally, we used the same mass cuts as for the previous analysis – the lower stellar mass limit comes from the SIMBA resolution and the upper limit from the halo mass cut (see Section 2.1). As before (Section 3.2) for all the galaxies showing a null SFR, we set $\log(\text{sSFR}/\text{yr}^{-1}) = -14$ and we compute the SFMS based on the galaxies with $\log(\text{sSFR}/\text{yr}^{-1}) > -10.8 + 0.3z$ (see Section 4.1). Using this DISPERSE skeleton, we investigate the overall trends of all galaxies (centrals and satellites) at redshift $z = 0$ among these two models and compare to our results from SIMBA.

Fig. 14 shows ΔsSFR versus filamentary distance d at $z = 0$ for SIMBA (grey), IllustrisTNG (blue), and EAGLE (orange). Errors on the running medians are indicated by the shaded regions.

In general, all models predict a strong departure towards quenched galaxies when within $\lesssim 100$ ckpc of a filament. However, the details of trends show significant differences. The decline in SIMBA is much

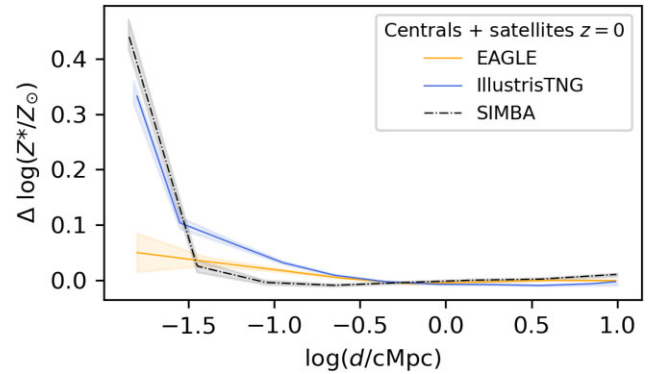


Figure 15. Distance from filaments dependence of the stellar metallicities' deviations from the MZR for all galaxies computed in EAGLE (orange line) and IllustrisTNG (blue line). The lines were obtained by binning the results in terms of distance and interpolating the corresponding medians. All the determinations are made for redshift $z = 0$. Galaxies in all simulations are more metal-enriched (mainly satellites) in the filaments proximity, but IllustrisTNG and SIMBA show strong increases close to filaments, while EAGLE shows only a modest increase.

more gradual than for EAGLE and IllustrisTNG, which show a very rapid transition from all galaxies being essentially on the SFMS to all galaxies being quenched. In SIMBA, this occurs for the satellites, but less so for the centrals (see Fig. 8). This suggests that the typical sSFR or quenched fractions in central galaxies ~ 100 ckpc away from filaments may be a good discriminator between models.

Fig. 15 presents the metallicity trends, investigating as before the deviation of the stellar metallicity from the stellar MZR with distance from the nearest filament. In this case, the differences are only strongly visible out to a few tens of kpc from the filament, and SIMBA and IllustrisTNG show substantial increases in Z_* while EAGLE shows almost none.¹ It is further interesting that the deviations from the global mean relations extend much farther out in sSFR than in Z_* , showing that the two quantities are not simply inversely correlated via some sort of stellar FMR, but rather have a more complex relationship. These predictions provide clear testable ways to distinguish between models if stellar metallicities can be measured for such samples.

To sum up, overall we see general agreement between the trends resulting from EAGLE, ILLUSTRISTNG and SIMBA in sSFR, and Z_* . Specifically, we find that galaxies close to filaments are less star-forming and more metal-enriched, though only satellites are expected to lie above the MZR predictions in this region (see Section 4.3). These results strengthen the hypothesis of more quenched galaxies in the filaments' proximity, as noticed in the previous sections (Sections 3–5). None the less, there are some distinct differences that could potentially be testable with present-day or upcoming large spectroscopic surveys. In the future, we will investigate how these trends are diluted when confronted with observational limitations such as redshift space distortions.

¹We note that the underlying MZR in these three models are quite different in both shape and amplitude, owing to differences in assumed yields, feedback efficiencies, and metal loading. It is beyond the scope of this work to examine in detail the origin of these variations; here, we aim to mitigate the effects of such differences by considering only the deviations from the MZR self-consistently computed within each simulation.

8 SUMMARY

Using SIMBA simulations and the cosmic web extractor DISPERSE, we have investigated how galaxy properties depend on their location with respect to the filaments spines of the cosmic web. We have done so at various redshifts from $z = 2 \rightarrow 0$, and have examined how these trends are governed by specific modes of feedback as implemented in SIMBA. We have specifically excluded the cosmic web within haloes of $M_h > 10^{13} M_\odot$ so as to focus on environments outside of galaxy groups. We also compared SIMBA's predictions with those from EAGLE and ILLUSTRISTNG results derived using the same methodology with the same mass cuts. The main findings of this work are summarized as follows:

(i) Central galaxies close to filaments have typically higher stellar mass and are surrounded by more satellites than those far away from filaments, similarly at all redshifts considered $z = 0, 1, \text{ and } 2$ (Figs 2 and 3), in agreement with various previous literature results (e.g. Chen et al. 2017; Malavasi et al. 2017; Kraljic et al. 2018). It is important to control for these variations in mass and halo occupancy in order to isolate the effects owing to the cosmic web environment. We do so by considering centrals and satellites separately, and by either normalizing to stellar mass or by computing deviations of quantities at a given M_* . This represents a novel aspect of this study since disentangling between centrals and satellites is very challenging in observational studies.

(ii) At redshifts $z = 0$ and 1, the sSFR or just sSFR is suppressed for satellites and centrals close to filaments, and increasing with distance. This trend has been reported before (e.g. Kuutma, Tamm & Tempel 2017; Poudel et al. 2017). We additionally note that this effect is considerably stronger for satellites and at later epochs, showing that satellites are more strongly impacted by the cosmic web environment over time. For instance, at redshift $z = 0$, satellites are typically fully quenched within several hundreds kpc of a filament and do not converge to the sSFR's of centrals until one reaches ~ 10 cMpc from filaments (Fig. 4). This shows that pre-processing of satellites is already prevalent in filaments at $z \lesssim 1$, prior to reaching group environments. The effects on centrals are also noticeable, particularly within $\lesssim 100$ ckpc of filaments. One can thus regard 100 ckpc as a rough scale over which filamentary environment impacts SF in galaxies.

(iii) The cold gas fractions, characterized in this study via M_{HI}/M_* and M_{H2}/M_* , show more subtle and challenging trends with the distance from the closest filaments (Fig. 5), especially for centrals. Broadly, cold gas is suppressed towards filament spines, increasingly so to lower redshifts as with sSFR, in qualitative agreement with Crone Odekon et al. (2018) and disagreement with Kleiner et al. (2017). However, centrals can be more or less suppressed in cold gas than satellites depending on distance. One aspect that may be confusing is that it can be difficult to associate particularly HI with any particular galaxy within a denser environment, as HI arises in relatively diffuse gas. Hence, a proper investigation of HI contents may require creating mock observations for a particular setup and conducting side-by-side analyses with data, which is beyond the scope here but will be feasible using upcoming multiwavelength radio surveys.

(iv) The stellar metallicity is higher close to filaments for both centrals and satellites, at all three redshifts considered (Fig. 6), in agreement with Winkel et al. (2021) and Donnan, Tojeiro & Kraljic (2022). However, we additionally note that the trend with distance is much steeper at $z = 2, 1$, and is diluted by $z = 0$. The trends for centrals and satellites are not markedly different.

(v) The quenched fraction and the elliptical fractions are both anticorrelated with distance to filament, for both satellites and centrals, generally tracking the trends for sSFR as expected. The quenched fraction trend fades out at redshift $z = 2$, while the elliptical fraction trend is more consistent at all three redshifts considered $z = 0, 1, \text{ and } 2$ (Fig. 7). At a given distance, satellites at $z = 0$ and 1 tend to be more quenched and elliptical. This is in spite of the fact that they are lower mass than the centrals (we have not controlled for stellar mass in this plot). Hence, cosmic web environment impacts both colour and morphology.

(vi) The trends noted above for sSFR are broadly similar when considering deviations from mean scaling relations rather than the quantities themselves (Fig. 8). This gives us confidence that the trends seen previously did not owe simply to trends with M_* , and are instead genuinely due to being close to a filament. However, there are more significant differences in the case of metallicity Z_* ; unlike for the overall metallicity Z_* for which we saw a clear increase towards filaments, once we control for the M_* dependence via the MZR, we now see no deviation from the mean MZR with distance for central galaxies, while satellites show strong deviations from the mean MZR only within $\lesssim 100$ ckpc (Fig. 10). Also, the trends in H_2 fraction with distance are not very strong when considering deviations from the mean $M_{\text{H2}}-M_*$ relation, indicating that the reduction in sSFRs close to filaments must owe primarily to a reduction in the SF efficiencies of those galaxies (Fig. 9).

(vii) We investigate whether the trends in sSFR owe to feedback or cosmic web growth by comparing amongst identical SIMBA runs with individual feedback modes turned off. We find that the predominant effect owes to the cosmic web, presumably via shock heating the gas to retard SF near filaments. However, the effects of feedback are not negligible; they add to the effects of LSS and increase the range out to which satellites are quenched at $z = 0$ by $\sim \times 2$ (Fig. 11). The bulk of this extra suppression comes from AGN feedback; SF feedback has a minor impact (Fig. 12).

(viii) While we have mostly excluded massive haloes from this analysis, we examine whether the impact of filaments is still noticeable around haloes with $M_h > 10^{13} M_\odot$ by comparing trends in sSFR versus halo-centric distance for galaxies near filaments and far from filaments. We find that the majority of the suppression of sSFR owes to the fact that these galaxies live around massive haloes. However, there are significant differences for the galaxies close to filaments feedback the massive haloes; they show a different pattern of sSFR suppression for centrals, and slightly more extended suppression for satellites (Fig. 13). Hence, location within the cosmic web generates an effect over and above that arising simply due to being close to a massive haloes.

(ix) We compare our SIMBA results to those from the EAGLE and IllustrisTNG simulations at $z = 0$, focusing on deviations from the mean sSFR and Z_* relations with mass, and considering centrals and satellites together. In general, all models show similar levels of sSFR suppression close to haloes, although SIMBA's trend is more gradual while EAGLE and IllustrisTNG show a very sharp drop in median sSFR at ~ 100 ckpc (Fig. 14). Meanwhile, Z_* shows a significant increase very close to filaments for IllustrisTNG and SIMBA, but such a trend is not seen in EAGLE (Fig. 15). These highlight possible avenues by which galaxy statistics relative to the cosmic web may provide discriminatory power between forefront simulations.

The overall distribution of galaxies with respect to filaments, specifically high-mass centrals with their accompanying low-mass satellites in the filaments' proximity can be explained by the environmental effects on the halo mass function (e.g. Alam et al. 2019).

The satellites' suppressed SF, enriched metallicity and suppressed gas content trends at fixed stellar mass (Section 4.1, 4.3, and 4.2) are consistent with a scenario where satellites close to filaments are quenched via H I reservoir depletion and lowered efficiency in converting H₂ into stars putatively owing to an increase in shock-heated gas near filaments. This also results in higher metallicities owing to the lack of infalling (relatively) pristine gas. The corresponding trends are considerably weaker for centrals, indicating that the cosmic web effects are less efficient in this case, possibly because centrals live within denser gas near the bottom of their haloes' potential wells.

SF suppression starts around $z \sim 2$, since environmental trends are not evident then, and if anything show a reversed trend in which all galaxies close to filaments have slightly higher sSFR's. At earlier epochs, we find results very similar to those at $z = 2$, so we did not explicitly show them. Given that gas depletion and SF suppression are mostly present around filaments even when feedback is excluded (Section 5), we argue that the interactions between satellites and the hot gas of cosmic web cause quenching via a combination of gas stripping, on shorter time-scales, and starvation, on longer time-scales. None the less, feedback has an additional non-negligible impact, providing a way to constrain models of (particularly) AGN feedback.

Overall, we find that the cosmic web plays a non-negligible role in shaping galaxy properties, though these effects are secondary to, i.e. weaker than, the mass effects. Our results generally agree with similar recent studies (e.g. Kraljic et al. 2018; Bhambhani et al. 2022; Malavasi et al. 2022) and provide new perspectives by clearly separating centrals and satellites, controlling for stellar mass, considering only galaxies within low-mass haloes and investigating the impact of various feedback scenarios. Observational results are required to test these predictions and potentially identify areas for improvements in simulations. Identifying the cosmic web ideally requires large-area spectroscopic surveys (although it may be possible to extract signals from the 2D cosmic web from photo- z 's), which exist now with SDSS and GAMA but will soon be greatly boosted with new facilities like Euclid (Cimatti et al. 2009; Refregier 2009; Laureijs et al. 2011), WEAVE (Dalton et al. 2012), PFS (Takada et al. 2014), 4MOST (de Jong et al. 2019), and DESI (DESI Collaboration et al. 2016). Combining these with multiwavelength surveys to characterize the various physical properties of galaxies, provides an exciting new frontier to explore how galaxy evolution models can be constrained using the cosmic web.

ACKNOWLEDGEMENTS

The authors thank the anonymous referee for insightful comments. The authors would also like to thank Katja Fahrion for helpful discussions and the developers of DISPERSE and CAESAR for making their codes public. This work was supported by the science and Technology Facilities Council (STFC). For the purpose of open access, the author has applied a Creative Commons Attribution (CC BY) licence to any Author Accepted Manuscript version arising from this submission.

DATA AVAILABILITY

The SIMBA simulation data and CAESAR galaxy catalogues are publicly available at <https://simba.roe.ac.uk>. The derived data and DISPERSE outputs underlying this article will be shared on reasonable request to the corresponding author.

REFERENCES

- Abazajian K. N. et al., 2009, *ApJS*, 182, 543
 Alam S., Zu Y., Peacock J. A., Mandelbaum R., 2019, *MNRAS*, 483, 4501
 Alpaslan M. et al., 2015, *MNRAS*, 451, 3249
 Anglés-Alcázar D., Özel F., Davé R., 2013, *ApJ*, 770, 5
 Anglés-Alcázar D., Özel F., Davé R., Katz N., Kollmeier J. A., Oppenheimer B. D., 2015, *ApJ*, 800, 127
 Anglés-Alcázar D., Faucher-Giguère C.-A., Kereš D., Hopkins P. F., Quataert E., Murray N., 2017, *MNRAS*, 470, 4698
 Appleby S., Davé R., Sorini D., Storey-Fisher K., Smith B., 2021, *MNRAS*, 507, 2383
 Aragón-Calvo M. A., van de Weygaert R., Jones B. J. T., 2010, *MNRAS*, 408, 2163
 Bahé Y. M., McCarthy I. G., Crain R. A., Theuns T., 2012, *MNRAS*, 424, 1179
 Bahé Y. M., Schaye J., Crain R. A., McCarthy I. G., Bower R. G., Theuns T., McGee S. L., Trayford J. W., 2017, *MNRAS*, 464, 508
 Baldry I. K., Balogh M. L., Bower R. G., Glazebrook K., Nichol R. C., Bamford S. P., Budavari T., 2006, *MNRAS*, 373, 469
 Behroozi P., Wechsler R. H., Hearin A. P., Conroy C., 2019, *MNRAS*, 488, 3143
 Beygu B., Kreckel K., van der Hulst J. M., Jarrett T. H., Peletier R., van de Weygaert R., van Gorkom J. H., Aragón-Calvo M. A., 2016, *MNRAS*, 458, 394
 Beyoro-Amado Z., Pović M., Sánchez-Portal M., Belay Tessema S., Getachew-Woreta T., Team Glace, 2021, in Pović M., Marziani P., Masegosa J., Netzer H., Negu S. H., Tessema S. B., eds, Vol. 356, Nuclear Activity in Galaxies Across Cosmic Time. p. 163
 Bhambhani P. C., Baldry I. K., Brough S., Hill A. D., Lara-Lopez M. A., Loveday J., Holwerda B. W., 2022, *MNRAS*, 522, 4116
 Bilicki M. et al., 2016, *ApJS*, 225, 5
 Bond J. R., Kofman L., Pogosyan D., 1996, *Nature*, 380, 603
 Bonjean V., Aghanim N., Douspis M., Malavasi N., Tanimura H., 2020, *A&A*, 638, A75
 Boselli A., Gavazzi G., 2006, *Publ. Astron. Soc. Pac.*, 118, 517
 Boselli A., Gavazzi G., 2014, *A&A Rev.*, 22, 74
 Castignani G. et al., 2022, *A&A*, 657, A9
 Catinella B. et al., 2010, *MNRAS*, 403, 683
 Chen Y.-C. et al., 2017, *MNRAS*, 466, 1880
 Cimatti A. et al., 2009, *Exp. Astron.*, 23, 39
 Codis S., Jindal A., Chisari N. E., Vibert D., Dubois Y., Pichon C., Devriendt J., 2018, *MNRAS*, 481, 4753
 Colless M. et al., 2001, *MNRAS*, 328, 1039
 Crone Odekon M., Hallenbeck G., Haynes M. P., Koopmann R. A., Phi A., Wolfe P.-F., 2018, *ApJ*, 852, 142
 Cui W. et al., 2018, *MNRAS*, 480, 2898
 Cui W., Davé R., Peacock J. A., Anglés-Alcázar D., Yang X., 2021, *Nat. Astron.*, 5, 1069
 Daddi E. et al., 2007, *ApJ*, 670, 156
 Dalton G. et al., 2012, in McLean I. S., Ramsay S. K., Takami H., eds, SPIE Conf. Ser. Vol. 8446, Ground-based and Airborne Instrumentation for Astronomy IV. SPIE, Bellingham. p. 84460P
 Darvish B., Sobral D., Mobasher B., Scoville N. Z., Best P., Sales L. V., Smail I., 2014, *ApJ*, 796, 51
 Davé R., 2008, *MNRAS*, 385, 147
 Davé R., Finlator K., Oppenheimer B. D., 2011, *MNRAS*, 416, 1354
 Davé R., Finlator K., Oppenheimer B. D., 2012, *MNRAS*, 421, 98
 Davé R., Thompson R., Hopkins P. F., 2016, *MNRAS*, 462, 3265
 Davé R., Anglés-Alcázar D., Narayanan D., Li Q., Rafieferantsoa M. H., Appleby S., 2019, *MNRAS*, 486, 2827
 Davé R., Crain R. A., Stevens A. R. H., Narayanan D., Saintonge A., Catinella B., Cortese L., 2020, *MNRAS*, 497, 146
 de Jong R. S. et al., 2019, *The Messenger*, 175, 3
 de Lapparent V., Geller M. J., Huchra J. P., 1986, *ApJ*, 302, L1
 Dekel A. et al., 2009, *Nature*, 457, 451
 DESI Collaboration et al., 2016, preprint (arXiv:1611.00036)
 Donnan C. T., Tojeiro R., Kraljic K., 2022, *Nat. Astron.*, 6, 599

- Dressler A., 1980, *ApJ*, 236, 351
- Dressler A., 1986, *ApJ*, 301, 35
- Driver S. P. et al., 2009, *Astron. Geophys.*, 50, 5.12
- Dubois Y. et al., 2014, *MNRAS*, 444, 1453
- Eardley E. et al., 2015, *MNRAS*, 448, 3665
- Finlator K., Davé R., 2008, *MNRAS*, 385, 2181
- Fujita Y., 2004, *Publ. Astron. Soc. Japan*, 56, 29
- Gabor J. M., Davé R., 2015, *MNRAS*, 447, 374
- Geller M. J., Huchra J. P., 1989, *Science*, 246, 897
- Giovannelli R. et al., 2005, *AJ*, 130, 2598
- Girelli G., Pozzetti L., Bolzonella M., Giocoli C., Marulli F., Baldi M., 2020, *A&A*, 634, A135
- Glowacki M., Elson E., Davé R., 2021, *MNRAS*, 507, 3267
- Gouin C., Aghanim N., Bonjean V., Douspis M., 2020, *A&A*, 635, A195
- Grand R. J. J. et al., 2017, *MNRAS*, 467, 179
- Grogin N. A., Geller M. J., 2000, *AJ*, 119, 32
- Hahn C. et al., 2019, *ApJ*, 872, 160
- Hasan F. et al., 2023, *ApJ*, 950, 14
- Hopkins P. F., 2015, *MNRAS*, 450, 53
- Hopkins P. F., Quataert E., 2011, *MNRAS*, 415, 1027
- Hoyle F., Vogeley M. S., Pan D., 2012, *MNRAS*, 426, 3041
- Iwamoto K., Brachwitz F., Nomoto K., Kishimoto N., Umeda H., Hix W. R., Thielemann F.-K., 1999, *ApJS*, 125, 439
- Jaffé Y. L., Smith R., Candlish G. N., Poggianti B. M., Sheen Y.-K., Verheijen M. A. W., 2015, *MNRAS*, 448, 1715
- Jones D. H. et al., 2004, *MNRAS*, 355, 747
- Katsianis A. et al., 2021, *MNRAS*, 500, 2036
- Kauffmann G., White S. D. M., Heckman T. M., Ménard B., Brinchmann J., Charlot S., Tremonti C., Brinkmann J., 2004, *MNRAS*, 353, 713
- Kleiner D., Pimbblet K. A., Jones D. H., Koribalski B. S., Serra P., 2017, *MNRAS*, 466, 4692
- Kotecha S. et al., 2022, *MNRAS*, 512, 926
- Koulouridis E., Gkini A., Drigga E., 2024, preprint (arXiv:2401.05747)
- Kraljic K. et al., 2018, *MNRAS*, 474, 547
- Kraljic K., Davé R., Pichon C., 2020, *MNRAS*, 493, 362
- Kreckel K. et al., 2011, *AJ*, 141, 4
- Kreckel K., Croxall K., Groves B., van de Weygaert R., Pogge R. W., 2015, *ApJ*, 798, L15
- Krumholz M. R., Gnedin N. Y., 2011, *ApJ*, 729, 36
- Kuutma T., Tamm A., Tempel E., 2017, *A&A*, 600, L6
- Laigle C. et al., 2016, *ApJS*, 224, 24
- Laigle C. et al., 2018, *MNRAS*, 474, 5437
- Laureijs R. et al., 2011, preprint (arXiv:1110.3193)
- Li Q., Narayanan D., Davé R., 2019, *MNRAS*, 490, 1425
- Lucero D. M., Carignan C., Elson E. C., Randriamampandry T. H., Jarrett T. H., Oosterloo T. A., Heald G. H., 2015, *MNRAS*, 450, 3935
- Maddox N., Hess K. M., Obreschkow D., Jarvis M. J., Blyth S. L., 2015, *MNRAS*, 447, 1610
- Maiolino R., Mannucci F., 2019, *A&AR*, 27, 3
- Malavasi N. et al., 2017, *MNRAS*, 465, 3817
- Malavasi N., Langer M., Aghanim N., Galárraga-Espinosa D., Gouin C., 2022, *A&A*, 658, A113
- Mannucci F., Cresci G., Maiolino R., Marconi A., Gnerucci A., 2010, *MNRAS*, 408, 2115
- Marinacci F. et al., 2018, *MNRAS*, 480, 5113
- Moster B. P., Somerville R. S., Maubetsch C., van den Bosch F. C., Macciò A. V., Naab T., Oser L., 2010, *ApJ*, 710, 903
- Moutard T. et al., 2016, *A&A*, 590, A102
- Muratov A. L., Kereš D., Faucher-Giguère C.-A., Hopkins P. F., Quataert E., Murray N., 2015, *MNRAS*, 454, 2691
- Naiman J. P. et al., 2018, *MNRAS*, 477, 1206
- Nelson D. et al., 2018, *MNRAS*, 475, 624
- Nelson D. et al., 2019, *Comput. Astrophys. Cosmol.*, 6, 2
- Noeske K. G. et al., 2007, *ApJ*, 660, L43
- Nomoto K., Tominaga N., Umeda H., Kobayashi C., Maeda K., 2006, *Nucl. Phys. A*, 777, 424
- Obreschkow D., Rawlings S., 2009, *MNRAS*, 394, 1857
- Oppenheimer B. D., Davé R., 2006, *MNRAS*, 373, 1265
- Pillepich A. et al., 2018, *MNRAS*, 473, 4077
- Pillepich A. et al., 2019, *MNRAS*, 490, 3196
- Planck Collaboration XIII, 2016, *A&A*, 594, A13
- Poggianti B. M. et al., 2017, *Nature*, 548, 304
- Postman M., Geller M. J., 1984, *ApJ*, 281, 95
- Poudel A., Heinämäki P., Tempel E., Einasto M., Lietzen H., Nurmi P., 2017, *A&A*, 597, A86
- Refregier A., 2009, *Exp. Astron.*, 23, 17
- Ricciardelli E., Cava A., Varela J., Quilis V., 2014, *MNRAS*, 445, 4045
- Rojas R. R., Vogeley M. S., Hoyle F., Brinkmann J., 2004, *ApJ*, 617, 50
- Salerno J. M. et al., 2020, *MNRAS*, 493, 4950
- Salés L. V., Navarro J. F., Theuns T., Schaye J., White S. D. M., Frenk C. S., Crain R. A., Dalla Vecchia C., 2012, *MNRAS*, 423, 1544
- Schaap W. E., van de Weygaert R., 2000, *A&A*, 363, L29
- Schawinski K. et al., 2014, *MNRAS*, 440, 889
- Schaye J. et al., 2015, *MNRAS*, 446, 521
- Schmidt M., 1959, *ApJ*, 129, 243
- Scodeggio M. et al., 2018, *A&A*, 609, A84
- Smith B. D. et al., 2017, *MNRAS*, 466, 2217
- Sorini D., Davé R., Cui W., Appleby S., 2022, *MNRAS*, 516, 883
- Sousbie T., 2011, *MNRAS*, 414, 350
- Sousbie T., Pichon C., Kawahara H., 2011, *MNRAS*, 414, 384
- Springel V., 2005, *MNRAS*, 364, 1105
- Springel V. et al., 2018, *MNRAS*, 475, 676
- Takada M. et al., 2014, *Publ. Astron. Soc. Japan*, 66, R1
- Tegmark M. et al., 2004, *ApJ*, 606, 702
- Trager S. C., Faber S. M., Worthey G., González J. J., 2000, *AJ*, 120, 165
- Tremonti C. A. et al., 2004, *ApJ*, 613, 898
- Tudorache M. N. et al., 2022, *MNRAS*, 513, 2168
- Urban O., Werner N., Allen S. W., Simionescu A., Mantz A., 2017, *MNRAS*, 470, 4583
- Vulcani B. et al., 2019, *MNRAS*, 487, 2278
- Wegner G. A., Salzer J. J., Taylor J. M., Hirschauer A. S., 2019, *ApJ*, 883, 29
- Weinberger R. et al., 2017, *MNRAS*, 465, 3291
- Wetzel A. R., Tinker J. L., Conroy C., 2012, *MNRAS*, 424, 232
- Wetzel A. R., Tinker J. L., Conroy C., van den Bosch F. C., 2013, *MNRAS*, 432, 336
- Williams R. J., Quadri R. F., Franx M., van Dokkum P., Labbé I., 2009, *ApJ*, 691, 1879
- Winkel N., Pasquali A., Kraljic K., Smith R., Gallazzi A., Jackson T. M., 2021, *MNRAS*, 505, 4920
- Zel'dovich Y. B., 1970a, *A&A*, 5, 84
- Zel'dovich Y. B., 1970b, *Astrophysics*, 6, 164
- Zheng H., Liao S., Hu J., Gao L., Grand R. J. J., Gu Q., Guo Q., 2022, *MNRAS*, 514, 2488
- Zolotov A. et al., 2015, *MNRAS*, 450, 2327

This paper has been typeset from a $\text{\TeX}/\text{\LaTeX}$ file prepared by the author.